Schweizerische Eidgenossenschaft
Confédération suisse
Confederazione Svizzera
Confederaziun svizra

Federal Department of the Environment, Transport, Energy and Communications DETEC

**Swiss Federal Office of Energy SFOE**
Energy Research and Cleantech Division

**Final report dated 31/03/2021**

# POST

# Plant Operation Stability Modeling

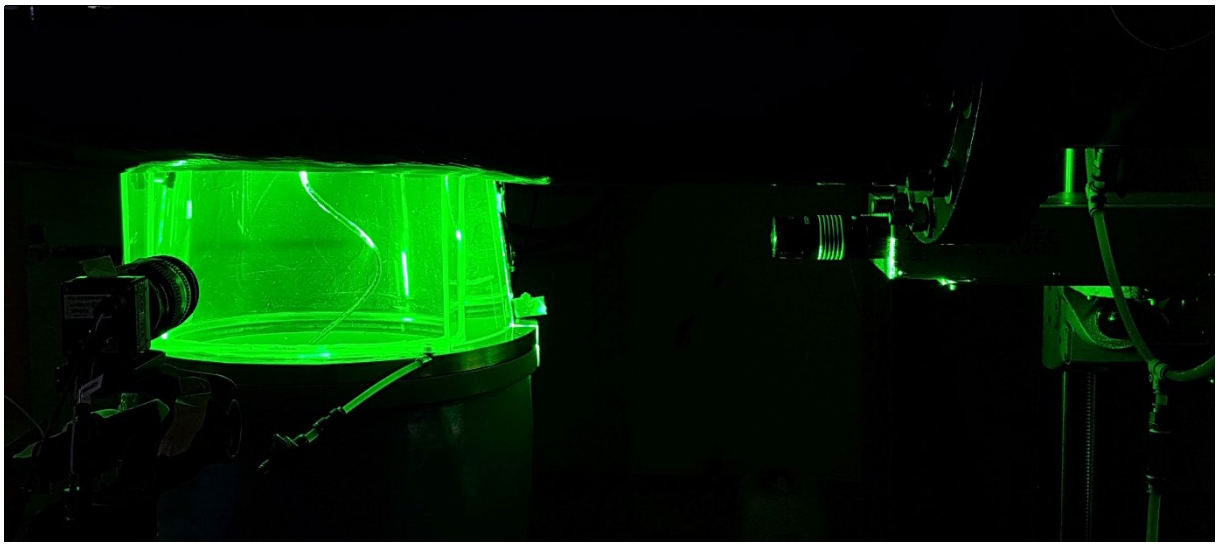

PIV measurement on the cavitation vortex rope of a Francis turbine in part load conditions.
**Source:** EPFL – PTMH 2020

**Date:** 31.03.2021

Location: Bern

**Publisher:**
Swiss Federal Office of Energy SFOE
Energy Research and Cleantech
CH-3003 Bern
www.bfe.admin.ch

**Subsidy recipients:**
EPFL - Technology Platform for Hydraulic Machines (PTMH)
(Former Laboratory for Hydraulic Machines)
Avenue de Cour 33 Bis CH-1007 Lausanne
https://ptmh.epfl.ch

**Authors:**
Ali Amini, EPFL - PTMH, ali.amini@epfl.ch
Elena Vagnoni, EPFL - PTMH, elena.vagnoni@epfl.ch

**SFOE project coordinators:**
Klaus Jorde, klaus.jorde@kjconsult.net
Michael Moser, michael.moser@bfe.admin.ch

SFOE contract number: SI/501943-01

# Zusammenfassung

Der Anteil der Wasserkraft an der gesamten Stromerzeugung im europäischen Stromnetz lag 2017 bei 15 %. In der Schweiz stammten im Jahr 2018 37,5 GWh des erzeugten Stroms aus Wasserkraft. Um die ehrgeizigen Ziele der Energiestrategie 2050 zu erreichen, müssen nicht nur die verborgenen Potenziale erschlossen, sondern auch die bestehenden Anlagen optimiert werden. Das bedeutet, dass von den rund 650 bestehenden Wasserkraftwerken viele in den kommenden Jahren neue Konzessionen beantragen müssen und ein erheblicher Modernisierungsbedarf besteht. Die Aufrüstung zu einer flexibleren Betriebsart wird von der Genauigkeit der Tools zur Bewertung der Strömungsstabilität abhängen, die im Rahmen dieses Forschungsprojekts entwickelt werden. Dieser Bericht fasst die durchgeführten experimentellen Kampagnen, die numerischen Simulationen und die wichtigsten Ergebnisse des Projekts zusammen.

In der ersten Versuchskampagne wurde das Modell einer Francis-Turbine auf dem PF1-Prüfstand des PTMH an der EPFL installiert. Der Prüfstand wurde mit einem Durchflussanregungssystem ausgestattet, das aus einem Drehventil und einer Pumpe mit variabler Drehzahl besteht und den Kreislauf über einen weiten Bereich von Frequenzwerten anregen kann. Es wurden Druckmessungen entlang des Hydraulikkreislaufs durchgeführt, um das hydroakustische Verhalten des Systems zu untersuchen und seine Eigenfrequenzen als Funktion des Betriebszustands der Maschine sowohl bei Teillast als auch bei Hochlast zu identifizieren. In dieser ersten Phase wurde festgestellt, dass der gewählte Testmodus für die Untersuchung von Kavitationsphänomenen geeignet ist, die für die Stabilität des Kraftwerks sehr relevant sind. Tatsächlich zeigt das getestete Turbinenmodell eine außergewöhnlich gut entwickelter Wirbelkern, die in einem breiten Bereich von Kavitationszahlwerten kavitiert. Dieses Ergebnis ermöglichte es, die zweite Phase der Messungen auf die Betriebsbedingungen zu fokussieren, die aufgrund des Auftretens von Kavitation im Diffusorkonus der Maschine anfälliger für Instabilität sind.

In der zweiten Phase der Tests wurde das gleiche Modell der Francis-Turbine auf dem PF3-Prüfstand des PTMH der EPFL installiert. Der erste Teil der zweiten Phase wurde wie die erste Phase durchgeführt. Auf diese Weise konnte überprüft werden, dass die hydroakustischen Parameter der Maschine in Abhängigkeit von den Betriebsbedingungen in beide Prüfständen einem ähnlichen Trend folgen. Die erzielten Werte waren jedoch in den beiden Tests leicht unterschiedlich. Für die erste Eigenfrequenz wurde ein maximaler Unterschied von 30 % festgestellt, der auf die unterschiedlichen Hydraulikkreise der beiden Prüfstände zurückzuführen ist. Zusätzlich zu den Tests des Erregersystems umfasste die zweite Kampagne Geschwindigkeitsmessungen im Diffusorkonus unter verschiedenen Betriebsbedingungen der Maschine, einschließlich Teillast und Hochlast. Zu diesem Zweck wurde die Particle Image Velocimetry (PIV) mit fluoreszierenden Partikeln durchgeführt. Dadurch konnten Messungen unter Kavitationsbedingungen durchgeführt werden, die auf der Titelseite abgebildet sind. Diese Messungen zeigten, wie sich das Geschwindigkeitsfeld im Diffusorkonus ändert, sobald eine Instabilität auftritt. Für die obere Teillastinstabilität wurde beobachtet, dass die Strömung in Abhängigkeit vom momentanen Kavitationsvolumen, das in der Messebene vorhanden ist, durch völlig unterschiedliche Strukturen gekennzeichnet sein kann. Die schnelle Dynamik dieser Strukturen führt zu großen Amplitudenwerten der Druckschwankung. Im Falle des Hochlastregimes wurden diese Geschwindigkeitsmessungen zur Erklärung des Strömungsverhaltens und der Strömungsvariationen herangezogen, die bei selbsterregten, durch große Amplituden gekennzeichneten Schwingungen des Kavitationsvolumens auftreten. Die zweite Testkampagne umfasste auch Visualisierungen der Hochgeschwindigkeitsströmung, die für eine grosse Bandbreite von Betriebsbedingungen durchgeführt wurden. Die Nachbearbeitung dieser Visualisierungen ermöglichte die Berechnung der hydroakustischen Parameter des Systems durch die Auswertung des Wirbelkernkavitationsvolumens. Transiente numerische 1-D-Simulationen des reduzierten Modells, das die gesamte Prüfstand umfasst, wurden in SIMSEN durchgeführt, um die wichtigsten hydroakustischen Parameter des Systems zu identifizieren und das dynamische Verhalten der Maschine sowohl unter Teillast- als auch unter

Volllastbedingungen vorherzusagen. Der Vergleich der gemessenen mit den von SIMSEN berechneten Eigenfrequenzen zeigt einige Diskrepanzen, die auf Unsicherheiten bei den Messungen und/oder bei der Berechnung des Kavitationsvolumens zurückzuführen sein könnten.

# Résumé

L'hydroélectricité représentait le 15 % de l'électricité totale produite dans le réseau électrique européen en 2017. En Suisse, 37.5 GWh de l'électricité produite provenaient de l'hydroélectricité en 2018. Pour atteindre les objectifs ambitieux de la Stratégie énergétique 2050, il faut non seulement saisir le potentiel caché, mais aussi optimiser les actifs actuels. Cela signifie que parmi les quelque 650 centrales de la flotte hydroélectrique existante, un grand nombre d'entre elles devront demander de nouvelles concessions au cours des prochaines années et d'importants besoins de modernisation seront requis. La modernisation vers une plus grande flexibilité des modes d'opération reposera sur la précision des outils d'évaluation de la stabilité de l'écoulement dont le développement est adressé dans le cadre de ce projet de recherche. Le présent rapport résume les campagnes expérimentales réalisées, les simulations numériques et les principaux résultats obtenus au cours du projet.

Dans la première campagne expérimentale, le modèle réduit d'une turbine Francis a été installé sur le banc d'essai PF1 de la PTMH de l'EPFL. La plateforme était équipée d'un système d'excitation de l'écoulement constitué d'une vanne rotative et d'une pompe à vitesse variable, qui peuvent exciter le circuit sur une large gamme de valeurs de fréquence. Des mesures de pression ont été effectuées le long du circuit hydraulique pour étudier la réponse hydroacoustique du système et identifier ses fréquences propres en fonction de l'état de fonctionnement de la machine à la fois à charge partielle et à forte charge. Au cours de cette première phase, il a été établi que le mode d'essai retenu convient à l'étude des phénomènes de cavitation, qui sont très pertinents pour la stabilité de la centrale. En fait, le modèle de turbine testé présente une torche exceptionnellement bien développée qui cavite sous une large gamme de valeurs de nombre de cavitation. Ce résultat à permis de focaliser la deuxième phase des mesures sur les conditions de fonctionnement qui sont plus sujettes à l'instabilité en raison de l'apparition de la cavitation dans le cône du diffuseur de la machine.

Dans la deuxième phase des tests, le même modèle de la turbine Francis a été installé sur le banc d'essai PF3 de la PTMH de l'EPFL. La première partie de la deuxième phase était comme celle de la première phase. Cela a permis de vérifier que les paramètres hydroacoustiques de la machine suivraient une tendance similaire en fonction des conditions d'opération dans les deux plateformes. Les valeurs obtenues étaient cependant légèrement différentes pour les deux essais. En ce qui concerne la première fréquence propre, une différence de 30% maximum a été observée, qui est attribuée aux différents circuits hydrauliques entre les deux plateformes. En plus des essais ave système d'excitation, la deuxième campagne comprenait des mesures de vitesse dans cône du diffuseur dans diverses conditions d'opération de la machine, y compris la charge partielle et la forte charge. Particle Image Velocimetry (PIV) avec des particules fluorescentes a été effectué à cette fin. Cela a permis d'effectuer des mesures dans des conditions de cavitation, dont une illustration est présentée sur la page de garde. Ces mesures ont révélé comment le champ de vitesse change dans le cône du diffuseur une fois qu'une instabilité se produit. Pour l'instabilité de la charge partielle supérieure, on a observé que, selon le volume de cavitation instantanée présent dans le plan de mesure, l'écoulement peut être caractérisé par des structures totalement différentes. La dynamique rapide de ces structures conduit à des valeurs de fluctuation de la pression de grande amplitude. Dans le cas du régime à forte charge, ces mesures de vitesse ont été utilisées pour expliquer le comportement de l'écoulement et les variations de débit qui se produisent pendant les oscillations auto-excitées du volume de cavitation caractérisé par des grandes amplitudes. La deuxième campagne d'essais comprenait aussi des visualisations de l'écoulement à haute vitesse réalisées pour un large domaine de conditions de fonctionnement. Le post-traitement de ces visualisations a permis de calculer les paramètres hydroacoustiques du système par

l'évaluation du volume de cavitation de la torche. Des simulations numériques transitoires 1-D du modèle réduit comprenant l'ensemble de la plateforme ont été effectuées dans SIMSEN pour identifier les principaux paramètres hydroacoustiques du système et prédire le comportement dynamique de la machine à la fois à charge partielle et à forte charge. La comparaison des fréquences naturelles mesurées avec celles calculées par SIMSEN révèle quelques écarts, qui pourraient être dus aux incertitudes dans les mesures et/ou au calcul du volume de cavitation.

# Summary

As a dispatchable Renewable Energy Source (RES), hydropower accounted for 15% of the total electricity generated in the European interconnected transmission system in 2017 (562.8 TWh out of 3,676.3 TWh). In Switzerland, 37.5 GWh (55.4%) of the produced electricity came from hydro in 2018. To reach the ambitious goals of the Energy Strategy 2050, not only does the hidden potential have to be seized, but also the current assets must be optimized. This means that among the 650 or so power stations in the existing hydropower fleet, many of them will have to apply for new concessions over the next years and significant refurbishment needs will emerge. Upgrading to more flexibility in operations will rely on the precision of the stability assessment tools that is sought to further develop in this research project. This report summarizes the performed experimental campaigns, numerical simulations and all main findings, which were achieved during the project.

In the first experimental campaign, a reduced-scaled model of a Francis turbine was installed on the PF1 test rig of the EPFL PTMH experimental facility. The test rig was equipped with a flow excitation system made of a rotating valve and a variable speed pump, which can excite the circuit across a wide range of frequency values. Pressure measurements have been performed along the hydraulic circuit to study the hydro-acoustic response of the system and identify its eigen frequencies depending on the operating condition of the machine both at part load and full load. During this first phase, it was established that the selected test case is suitable for the study of the cavitation phenomena, which are highly relevant to the stability of the power plant. In fact, the tested turbine model presents an exceptionally well-developed vortex rope that cavitates under a relatively large range of cavitation number values. This focalizes the second phase of the measurements on the operating conditions that are more prone to instability due to the appearance of cavitation in the draft tube.

In the second phase of the experiments, the same Francis turbine model was installed on the EPFL PTMH PF3 test rig. The first part of the second phase was like that of the first phase. This allowed verifying that the hydro-acoustic parameters of the machine would follow a similar trend with the operating conditions on both test rigs. The obtained values, however, were slightly different for the two tests. Concerning the first eigen frequency, a difference of maximum 30% was observed, which is attributed to the different layouts of the two test rigs. In addition to the excitation test, the second campaign included velocity measurements in the draft tube under various operating conditions including part load and full load. Particle Image Velocimetry (PIV) with fluorescent particles was implemented for this purpose. This allowed performing measurements under cavitation conditions, an illustration of which is shown on the cover page. These measurements revealed how the velocity field changes in the draft tube once an instability occurs. It has been observed for the upper part-load instability that depending on the instantaneous cavitation volume present in the measurement plane, the flow might take totally different structures. The fast dynamics of these structures leads to fluctuating pressure values of high-amplitude oscillations. In case of the full-load regime, these velocity measurements have been used to explain the flow behavior and discharge variations that occur during the self-excited high-amplitude oscillations of the cavitation volume. The second campaign included high-speed flow visualizations performed for a wide range of operating conditions. Post-processing of these visualizations enabled the computation of the hydro-acoustic parameters of the system by the evaluation of the cavitation volume of the vortex rope. 1-D transient numerical simulations of the reduced-scale model including the entire

test rig have been performed in SIMSEN to identify the key hydro-acoustic parameters (i.e. the bulk viscosity, cavitation compliance and mass flow gain factors) of the system and predict the dynamic behavior of the machine at both part-load and full-load. Comparing the measured natural frequencies with those computed by SIMSEN reveals some degrees of discrepancies, which might be due to the uncertainties in the measurements or the computation of the cavitation volume in the draft tube for instance.

# Main findings

The main findings of the project may be summarized as follows:

- The unique opportunity of performing measurements on the same Francis turbine in two different test rigs (EPFL PTMH PF1 & PF3) proved that although not taking the same values, the hydro-acoustic parameters of the machine follow similar trends with variations in the operating conditions independent of the test-rig. A difference of maximum 30% is observed in the value of the first natural frequency measured on the two test rigs, which is explained by the different layouts of the two test-rigs.
- Concerning the part-load regime, it is observed that the cavitation vortex rope in the draft tube may break into an elliptical shape if the amount of cavitation exceeds a critical threshold. This gives rise to the upper part-load instability, which is associated with high amplitude and high frequency vibrations in the hydraulic circuit. Velocity measurements show that under these conditions, the draft tube flow experiences totally different structures that vary with time and lead to the pulsating behavior.
- In contrast to the previous studies in literature, where the full load regime is associated with an axisymmetric cavitation vortex rope in the draft tube, this specific Francis turbine shows a peculiar behavior. At relatively high Thoma number values, the mentioned cavitation structure is quite small with a helical shape and precessing motion like that observed in the part-load regime. The reason of this phenomenon is yet to be determined.
- In case of the full-load instability associated with self-excited oscillations at high discharge values, it is observed that for this specific Francis turbine, it is not possible to establish a clear correlation between the swirl number and the self-excited frequency. This is most probably due to the strong dependencies that were observed between the machine behavior and the hydraulic head and the Thoma number, which cannot be represented by the Swirl number.

# Contents

# 1 Introduction

## 1.1 Background information and current situation

By 2030, the European Union is targeting to have at least 32% of its energy from renewable sources. Longer-term scenarios show an even more drastic de-carbonization with significant contributions from variable wind and solar energy in the electrical power system (EPS). Following these changes, a considerable mismatch between the power generation and consumption will occur, which must be compensated to guarantee the grid stability. In this context, hydropower units can play a key role to support the electrical grid by balancing consumption and production thanks to their capability to perform a flexible operation. However, to achieve this flexibility, hydraulic turbines are required to operate in non-optimal conditions. For Francis turbines, the acceptable operating range is limited by the drastic decrease of the turbine efficiency or the development of flow instabilities inducing cavitation and pressure pulsations risking damage and reducing the life span of the unit. Indeed, a comprehensive study of Francis turbines stability is required to predict the occurrence and behavior of the unsafe flow phenomena.

Numerous efforts have been undertaken so far by the research community to understand the underlying physical mechanisms causing and sustaining these flow instabilities. In addition, 1-D hydro-acoustic models have been developed to simulate the two-phase flow and its impact on the operational stability of the power plant. These models are based on the experimental determination of the relevant physical parameters performed during reduced-scale model tests at the EPFL Technology Platform for Hydraulic Machines (EPFL, PTMH). The major remaining challenge is how to transpose the results of these measurements and simulations to the full-scale prototype machines. This has recently been achieved for one of the demonstrators in the HYPERBOLE research project (ERC/FP7-ENERGY-2013-1-Grant 608532) [1], [2], [3] and [4]. However, to prove the validity of the approach and to assess the influence of the plant layout and the turbine geometry, it is essential to repeat similar operations on one or several other test cases.

## 1.2 Purpose of the project

The goal of this project is to accurately predict the stability of a specific hydropower plant, and throughout the process, to gain knowledge for applying this successfully to other cases, independent of their layout or the geometry of their generating units, with existing and already commercialized 1-D hydro-acoustic simulation tools (SIMSEN). This is tackled by performing two experimental campaigns on a reduced-scale model of a 9-MW Francis turbine prototype and 1-D numerical simulations in SIMSEN.

## 1.3 Objectives

The first experimental campaign investigates the hydro-acoustic response of the hydraulic circuit to identify the key acoustic parameters and establish their dependence on the geometrical and hydraulic parameters. These results will be fed into the 1-D numerical simulations to achieve the prediction of the turbine stability. The second experimental campaign re-assesses the findings of the first experimental campaign by repeating the excitation and pressure measurements in a second test test rig of EPFL PTMH to investigate the influence of the hydraulic circuit on the hydro-acoustic parameters. However, the main part of the second experimental campaign consists of 2-D laser-pulsed Particle Image Velocimetry (PIV) measurements with fluorescent particles in the draft tube of the tested turbine. This technique enables to measure velocity in the absence and presence of cavitation and compare them. These measurements are aimed at identifying the pressure excitation source induced by the vortex rope in the draft tube at both part-load and full-load operations. In addition, the results of the project are

targeted to lead to an improvement of the existing modules of hydro-acoustic stability assessment in SIMSEN software.

# 2 Description of the experimental facility

## 2.1 Instrumentation

Two experimental campaigns have been performed within the framework of this project. The first was performed in 2019 on the PF1 test rig and the second in 2020 on the PF3 test rig of EPFL PTMH. The measurements are carried out on a reduced-scale physical model of a Francis turbine with a specific speed $\nu = 0.33$ , which is defined as follows:

$$\nu = \omega \cdot \frac{Q^{1/2}}{\pi^{1/2} \cdot (2E)^{3/4}} \tag{1}$$

The reduced-scale model includes the upstream inlet pipe, the spiral case, the runner with a reference diameter $D = 0.35$ m , and the draft tube consisting of the cone, the elbow and the diffuser. A 300 kVA DC generator connected to the model runner regulates the rotational speed. The specific hydraulic energy in the closed-loop test rig is provided by a vertical 900 kW pump during the first experimental campaign and by two parallel 300 kW centrifugal pumps in the second experimental campaign. In both experimental campaigns, the test rig has been equipped with a flow excitation system made of a rotating valve and a variable speed pump to excite the test rig across a wide range of frequencies, as shown in Figure 1. This excitation system is fully described in [5, 6]. It features a KSB Movichrom G 15/5 pump, a custom-made rotating valve driven by a variable speed motor and an accumulator. The pump allows for the adjustment of the amplitude of the discharge pulsations, the rotating valve allows for the control of the pulsation frequency, and the accumulator, placed between the pump and the valve, limits the interference of the pump driving the excitation flow with the test rig. The frequency of the rotating valve increases from 1 Hz to 6 Hz by following a linear function. A typical time history of the pulsation frequency is presented in Figure 2 for a given operating point.

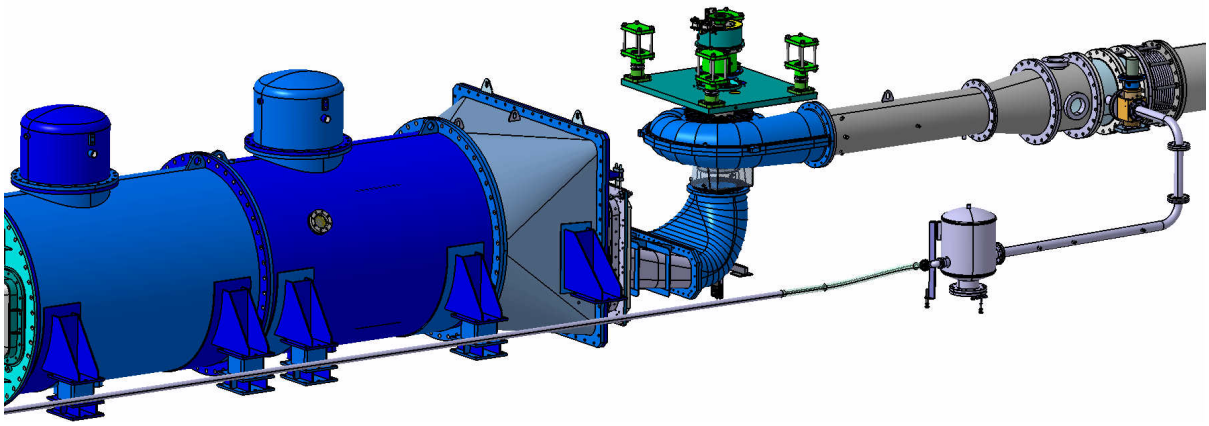

Figure 1: Experimental set-up and the excitation system installed on the PF3 EPFL PTMH test rig (second experimental campaign).

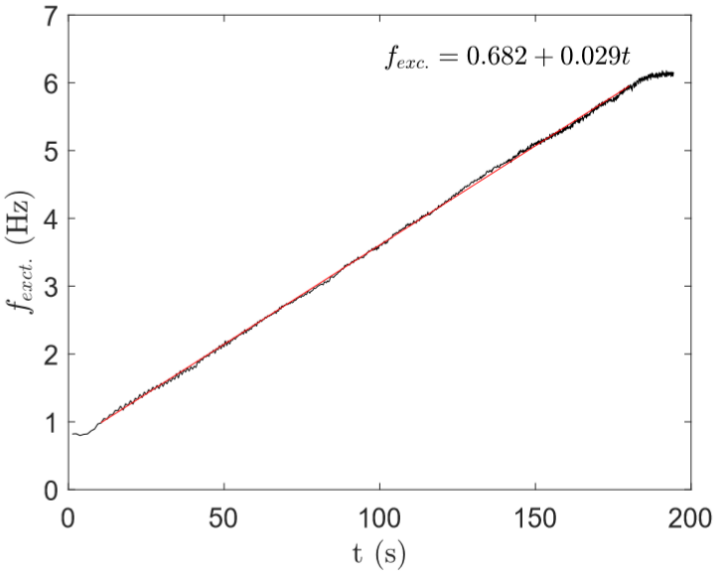


Figure 2: Time history of the excitation frequency.

During the first experimental campaign, wall pressure measurements were performed in 14 locations all along the test rig pipes, while in the second phase, the number of sensors were reduced to 10, which are shown in Figure 3. The wall pressure fluctuations are measured by flush-mounted piezo-resistive pressure sensors. These sensors feature 0–5 bar pressure measurement range with a maximum relative measurement uncertainty of 0.7 %. The sampling frequency is set to 1 kHz and a ~230 s time window of measurements is recorded for a typical excitation test.

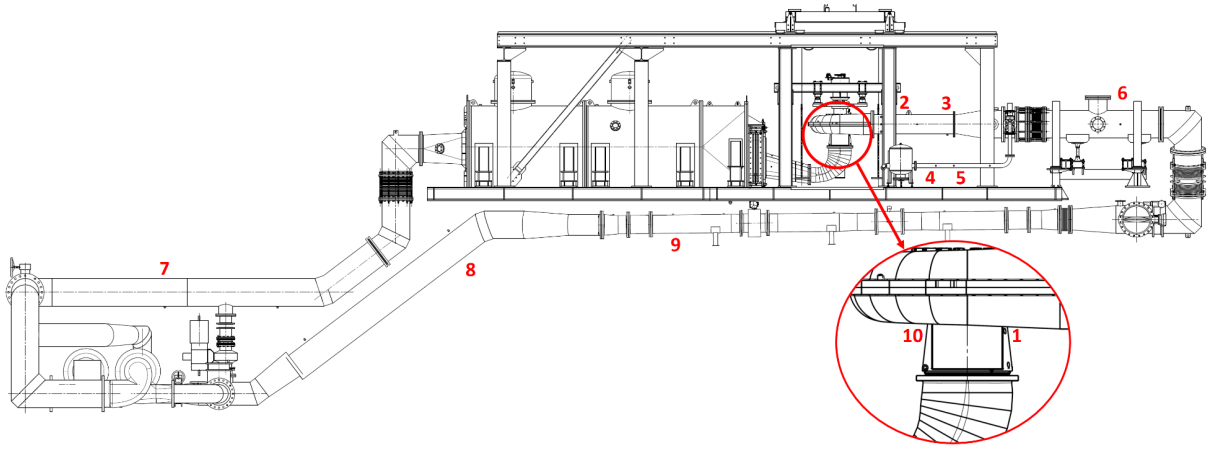


Figure 3: Side-view of the EPFL PTMH PF3 test rig for reduced-scale model tests equipped with pressure sensors.

Both experimental campaigns include high-speed visualizations of the cavitation vortex rope at both part-load and full-load conditions. The visualizations are achieved by the transparent Plexiglass cone of the draft tube below the runner. To avoid light distortions due to the curved surface of the draft tube, a rectangular water box was attached to it. The videos are recorded using a high-speed camera (Photron FastCam Mini 200) at image acquisition rates varying between 500 to 10,000 frames per second and a resolution of 1024 pixels by 1024 pixels. A 90% uniform LED screen (PHLOX LEDW-BL-550X400-MSLLUB-Q-1R-24V) of 500 mm x 400 mm size and 7000 cd $m^{-2}$ luminescence is installed as a backlight

to enhance the contrast between the gaseous and liquid phases. Illumination is improved by two 800 W continuous lights installed at the front and side. The camera is placed parallel to the water box face and is used to measure the volume of the cavitation vortex rope. A snapshot of one of these videos is shown in Figure 4, which depicts the cavitation vortex rope breakdown in the part-load condition.

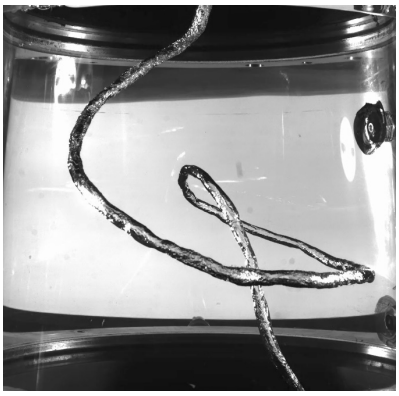

Figure 4: Vortex rope breakdown in the draft tube of the Francis model turbine operating in part-load condition (second experimental campaign)

The second experimental phase includes velocimetry tests, which were executed by implementing a laser-pulsed PIV setup to measure 2-D velocity fields in the draft tube on three different planes: two horizontal and one meridional. A schematic of these measurement planes is illustrated in Figure 5. For these PIV tests, fluorescent particles were used. In comparison to normal particles, the fluorescent ones are more expensive and more difficult to handle. Nevertheless, these particles allow performing PIV measurements under cavitation conditions, which is not feasible with the normal particles due to the extensive amount of laser light reflections from the cavity surface. For each operating condition, a sufficiently large number of images has been acquired so that the results become statistically independent from the number of samples. For each test condition, synchronous pressure measurements in the draft tube are also recorded. This allows further applying phase averaging to the obtained velocity fields based on the vortex procession motion.

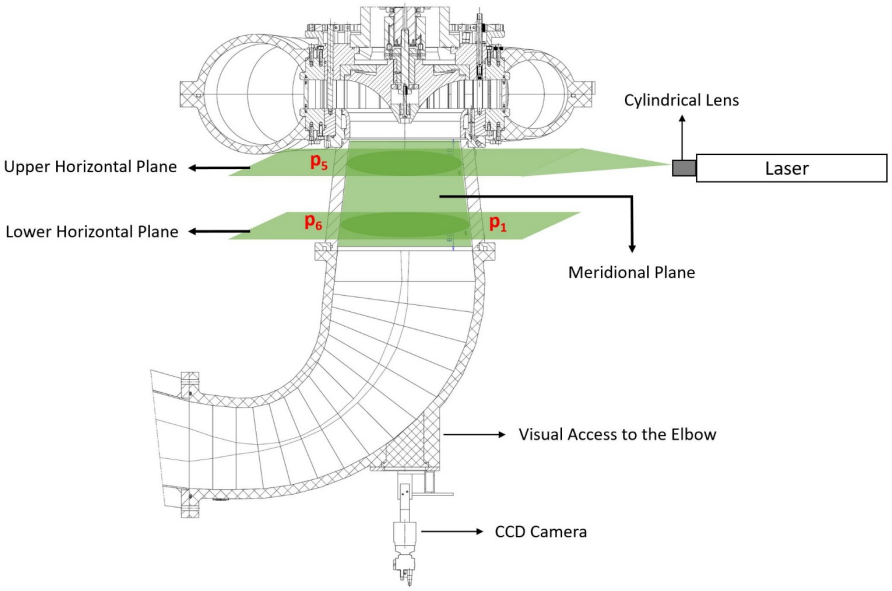


Figure 5: Schematic of the PIV measurements setup

## 2.2 Operating conditions

A wide range of operating conditions have been tested during the two experimental campaigns by changing the IEC speed factor $n_{ED}$, the IEC discharge factor $Q_{ED}$, the Froude number $Fr$, and the Thoma number $\sigma$.

These parameters are defined as follows:

$$n_{ED} = \frac{nD}{\sqrt{gH}} \; ; \quad Q_{ED} = \frac{Q}{D^2\sqrt{gH}} \; ; \quad Fr = \sqrt{\frac{H}{D}} \; ; \quad \sigma = \frac{NPSE}{gH} \tag{2}$$

Where $n$ is the rotational speed of the runner, $Q$ the discharge, $H$ the net head, $D$ the low-pressure diameter of the runner, $g$ the gravity acceleration and $NPSE$ the Net Positive Suction Specific Energy.

The experiments at different operating conditions have been performed as follows:

- Measurements of the pressure fluctuations with the excitation system at both part-load and full-load operations for the identification of the eigen frequencies and the key hydro-acoustic parameters.
- Measurements of the pressure fluctuations and flow visualization without the excitation system at both part-load and full-load to measure the cavitation volume in the vortex rope to compute the related mass-flow-gain factor $\chi$, as defined in equation (3).

  $$\chi = -\frac{\partial V_c}{\partial Q_1} \tag{3}$$

  Where $V_c$ is the cavitation volume of the vortex rope and $Q_1$ is the flow discharge at the turbine runner outlet.
- Measurements of the pressure fluctuations without the excitation system at full-load conditions to study of the instability onset.
- Measurement of the pressure fluctuations and flow visualization with the excitation system at one operating point at full-load to study the effect of the excitation system on the stability of the vortex rope at full-load.
- A large set of velocity measurements in the draft tube in order to correlate the machine behavior to the velocity fields. These include both part-load and full-load conditions, with and without the excitation systems, and in both cavitation and non-cavitation flow regimes. These velocity fields will be employed to determine the source of excitation induced by the vortex rope.

# 3 Procedures and methodology

## 3.1 Determination of the hydro-acoustic parameters

To predict the hydro-acoustic response of the machine and the stability of the system, the 1-D numerical model of the EPFL PTMH test rig PF1 and PF3 as well as the reduced-scale turbine model are required. For this purpose, the SIMSEN software is used, in which mass and momentum conservation equations are modelled according to their electrical equivalent, as presented in [7] and [8]. The SIMSEN components representing the test rig proposed by Landry et al. in [5] are illustrated in Figure 6 for the PF1 and Figure 7 for the PF3.

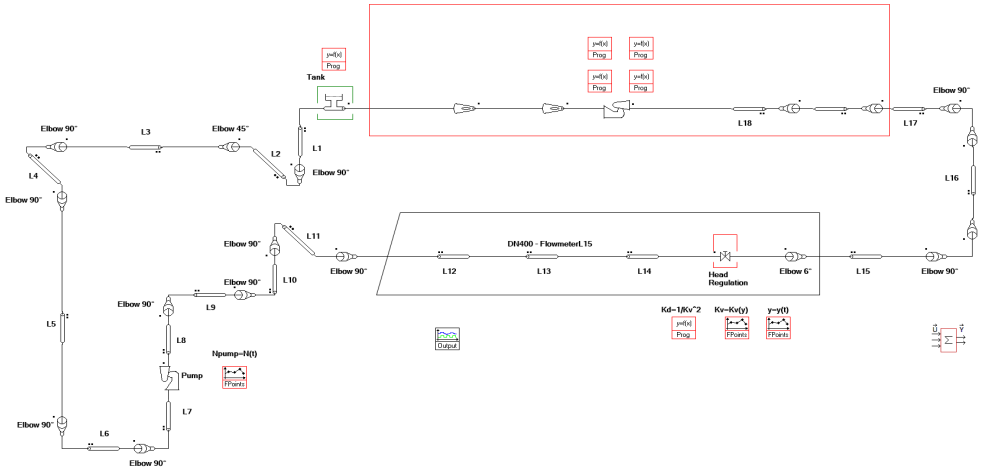


Figure 6: SIMSEN model of the PF1 EPFL PTMH test rig.

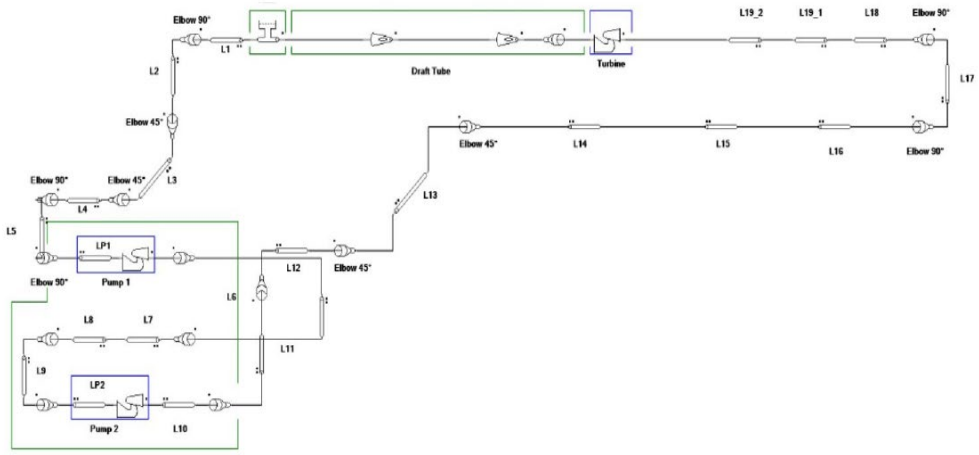


Figure 7: SIMSEN model of the PF3 EPFL PTMH test rig.

The integrated dynamic behavior of the whole test rig is simulated in the time domain through a set of first-order nonlinear ordinary differential equations. As detailed in reference [9], the eigenvalues of the complete system are calculated by performing a linear approximation of these equations. The main geometrical dimensions and the characteristics curves of the Francis turbine investigated in the experimental campaigns are given as an input to the turbine element in SIMSEN to correctly simulate the test rig and the machine operation. Alligné et al. [10] present the 1-D SIMSEN hydro-acoustic model of the cavitation in the draft tube cone. This model required the following inputs: the pipe viscosity $\mu'_{pipe}$, the dilation or the bulk viscosity $\mu''$, the mass flow gain factor $\chi$, and the wave speed $a$, which are computed based on the experimental results and the corresponding modal analysis. To calculate the mentioned parameters, one may implement one of the following two methods:

## METHOD 1: Iteration with the 1-D numerical model

This method is well suited for the prediction of the hydro-acoustic response of the system in case there are no direct measurements of the cavitation volume of the vortex rope [3], [4] and [12]. The eigen frequency is computed by modal analysis of the experimental data, and it is used as a reference to initialize the SIMSEN simulation and the calculation of the hydro-acoustic parameters. The SIMSEN model takes as input the hydro-acoustic parameters and gives as output the eigen frequency corresponding to the simulated operating condition. To have a good agreement between the

experiments and the numerical simulations, it is important to have an accurate estimation of the hydro-acoustic parameters. The wave speed can be expressed as a function of the swirl number $S$ through a regression method on the experimental data, which allows computing the non-dimensional wave speed $\Pi$.

$$\Pi = Ae^{B \cdot S} = \frac{\rho \cdot a^2}{p - p_v}$$
$$S = n_{ED} \frac{\pi^2}{8} \left( \frac{1}{Q_{ED}} - \frac{1}{Q_{ED,0}} \right) \quad (4)$$

Where $A$ and $B$ are the regression coefficients, $\rho$ the water density, $p$ is the pressure in the draft tube cone and $p_v$ the vapor pressure. $Q_{ED,0}$ is the IEC discharge coefficient at zero swirl. The cavitation compliance $C_c$, representing an additional compressibility caused by cavitation is calculated as follows:

$$C_c = \frac{\partial V_c}{\partial h} = \frac{1}{H} \frac{\partial V_c}{\partial \sigma} \approx \frac{g V_{cone}}{a^2} \quad (5)$$

Where $V_c$ is the cavitation volume, $h$ the piezometric head, and $V_{cone}$ the volume of the draft tube cone. Therefore, by knowing the wave speed and the volume of the draft tube cone, the cavitation compliance can be estimated. It follows that the cavitation volume can be also computed:

$$V_c = \int C_c(\sigma) d\sigma \quad (6)$$

Therefore, both the mass flow gain factor $\chi$ and the void fraction $\beta = V_c / V_{cone}$ can be also estimated. The pipe viscosity is computed as:

$$\mu'_{pipe} = 2.17 \cdot 10^6 \cdot f_0^{-0.879} \quad (7)$$

where $f_0$ is the first eigen frequency of the system. The bulk viscosity can be estimated with a theoretical relation as in [3]:

$$M'' = \frac{\mu'' \cdot f_0}{p - p_v} = \Pi^2 \cdot (1 - \beta)^2 \frac{\rho_v}{\rho} \quad (8)$$

By performing SIMSEN numerical simulation, the wave speed can be found by iteration with the dichotomy method [3] with a tolerance of 0.05 Hz to obtain a numerical natural frequency equivalent to the experimentally measured frequency. Before performing the iterative process for the identification of the wave speed, it is imperative that the SIMSEN model is stabilized at the values of the discharge and head of the experiment of reference. These two parameters are driven by the pump that supplies the head in the closed circuit and by the opening angle of the guide vanes. The values of the wave speed in the cone of the draft tube do not play a role in the stabilization.

## METHOD 2: Calculation of the cavitation volume

If the cavitation volume $V_c$ can be estimated by image-processing, the cavitation compliance can be directly computed by Eq. (6) so the wave speed by solving Eq. (5) and the non-dimensional wave speed by Eq. (4). All the other hydro-acoustic parameters can be estimated as explained in Method 1. The computation of the mass flow gain factor $\chi$ is firstly made; then, the introduction of the void fraction $\beta$ and the cavitation compliance $C_c$ yield to calculate the wave speed $a$ and the bulk viscosity $\mu''$. Considering that the discharge variation is not measured while recording the cavitation volume variations in the draft tube, a viable way to numerically compute the derivative is the following:

$$\chi = -\frac{\partial V_c}{\partial Q} = -\frac{\Delta V_c}{\Delta Q}\bigg|_{\sigma} \quad (9)$$

With $\Delta V_c$ and $\Delta Q$ being calculated for two volumes and two discharges associated with two consecutive values of $Q$ for a fixed $\sigma$. In parallel to the mass flow gain factor, the void fraction $\beta$ and the cavitation compliance $C_c$ may be computed as well. For $\beta$ the calculations are straightforward, with the introduction of the draft tube cone volume $V_{cone} = 0.0423\ \text{m}^3$. Concerning the cavitation compliance, the procedure is in principle like that for $\chi$. In fact, since a fixed operating point corresponds to a single volume value, the numerical derivative may be calculated as follows:

$$C_c = -\frac{1}{H}\frac{\partial V_c}{\partial \sigma} = -\frac{1}{H}\frac{\Delta V_c}{\Delta \sigma}\bigg|_Q \tag{10}$$

With $\Delta V_c$ being calculated for two volume values associated with two consecutive values of $\sigma$ for a fixed value of $Q$. Regarding the bulk viscosity, the determination of $\mu''$ is feasible by computing firstly $M''$ via Eq. (8) and, then, resolving for $\mu''$ using the hydraulic circuit natural frequency previously determined.

## 3.2 Dynamic modal analysis

Following the methodology proposed by Favrel et al. [6], a dynamic modal analysis is performed for each operating point of the two experimental campaigns. The pressure transducer signals are divided into several time windows whose maximum length ($T$) is calculated according to the following criterion:

$$T \leq \sqrt{\frac{2}{\nu_{\text{ramp}}}} \tag{11}$$

Where $V_{ramp}$ is the variation rate of the pulsation frequency of the rotating valve. The variation rate of the frequency is around 0.029 Hz·s$^{-1}$, which leads to a window length of 8.3 s. A 50% overlap is then applied to highlight the evolution of the excitation frequency. For each time window, which corresponds to an almost constant excitation frequency, a Hann window is applied to the pressure fluctuations, and then, the auto-power spectrum density function $G_{xx}$ is computed for that window. In Figure 8, an example of the waterfall diagram of the influence of the test rig response on the excitation frequency together with the phase shift along the test rig at full-load condition is presented. Two frequency values can be clearly identified as the eigen frequencies of the test rig, $f_0 = 2.6$ Hz and $f_1 = 5.9$ Hz. The procedure is applied to all investigated operating conditions to calibrate the SIMSEN model to compute the hydro-acoustic parameters and to predict the machine stability on an extended range.

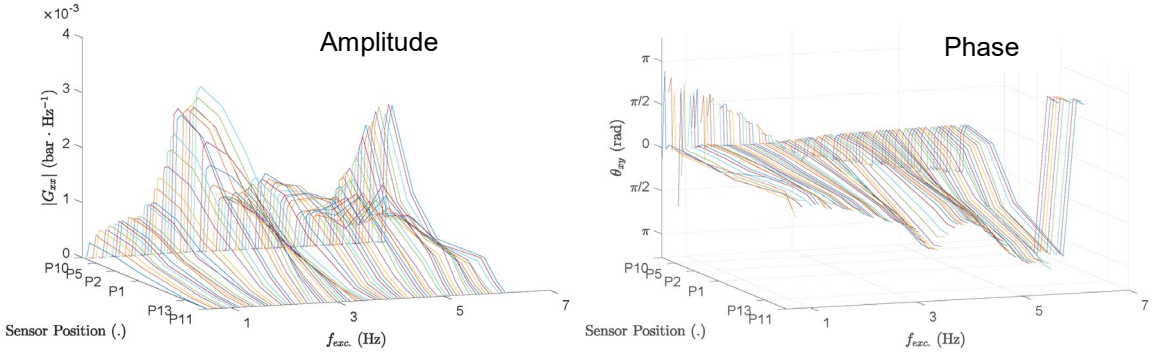


Figure 8: PF1 response as a function of the excitation frequency at $n_{ED} = 0.343$, $Q_{ED} = 0.249$, $Fr = 7.79$ and $\sigma = 0.07$.

## 3.3 Cavitation volume estimation

An image-processing algorithm is used to estimate the volume of the cavity in the draft tube in the high-speed visualizations. The first step is to find the location of the left and right edges of the cavitation vortex on each horizontal cut.

The flowchart shown in Figure 9 depicts the algorithm realizing this task.

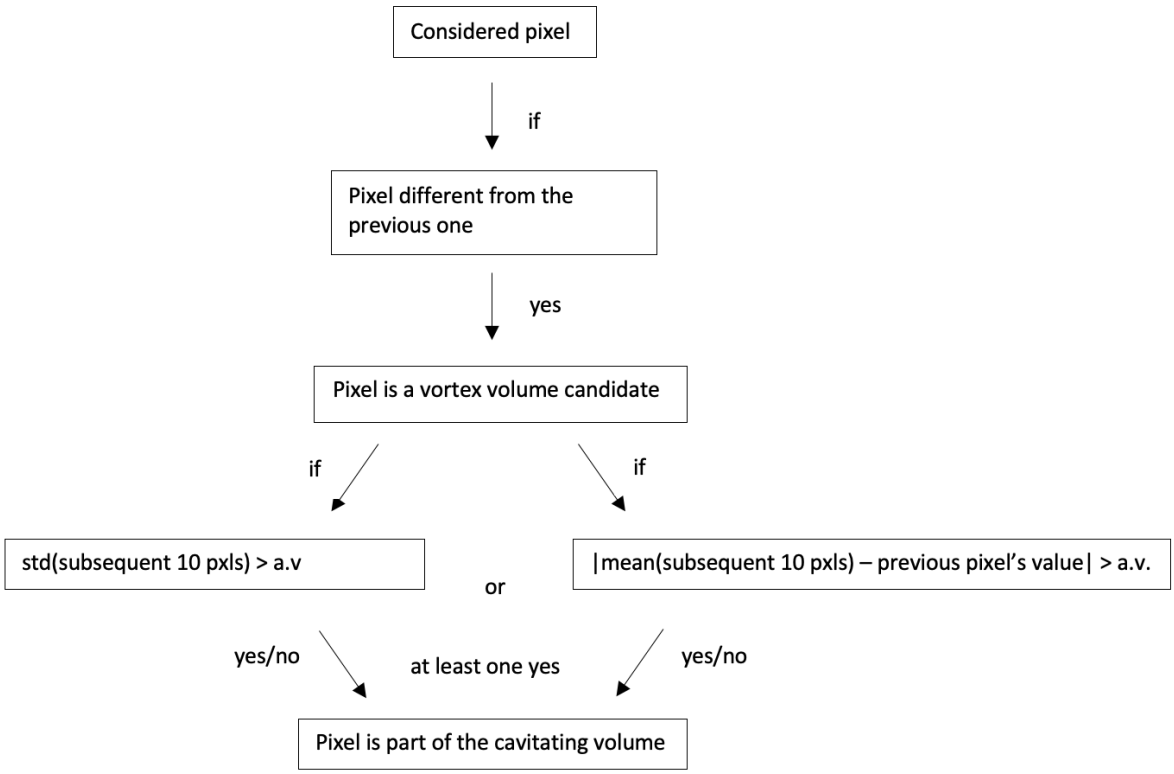


Figure 9: Flowchart to find the vortex volume in the central region (a.v.: arbitrary value).

Applying the edge detection routine results in an accurate 2-D identification of the vortex. The binary representation gives the advantage of a simple distinction between the whole cavitation volume and the liquid phase. To overcome the difficulties arising from separated and non-horizontal vortex ropes, the volume calculation is first performed to compute the volume of the hypothetical entire and unbroken vortex rope. Then, every internal black zone is subtracted. The concept of calculating a vortex volume starting from a 2-D representation relies on two fundamental notions: the vortex is assumed to be a circular sectioned cylinder with its core lying along a 3-D center line and its section always perpendicular to this line.

Knowing the centerline inclination and the section diameter for every point, one could detect two vortex boundaries as well as the centerline, as shown in Figure 10. Summing the tiny cylinders gives the vortex volume, computed without considering the empty areas caused by holes in the volume or by divided vortex ropes. The last step is to identify and subtract the excess volume.

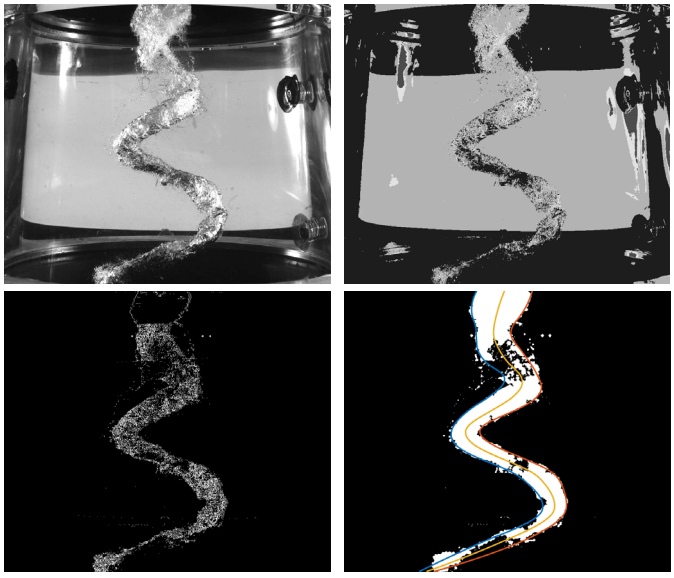

Figure 10: Image processing steps: vortex identification and consolidation followed by boundaries and centerline computation.

## 3.4 Velocity profiles with PIV

To obtain a better insight of the flow structures in the draft tube cone, 2-D planar PIV technique was implemented on three different planes in the draft tube (Figure 5). The use of fluorescent particles allows performing the velocity measurements on a wide range of flow conditions including cavitation flows. This includes part-load, full-load, cavitation, non-cavitation, with or without hydraulic excitation, various values of $n_{11}$, $Q_{11}$, head, dissolved oxygen, etc. A typical cavitation vortex rope, which forms in part load conditions, is depicted in Figure 11.

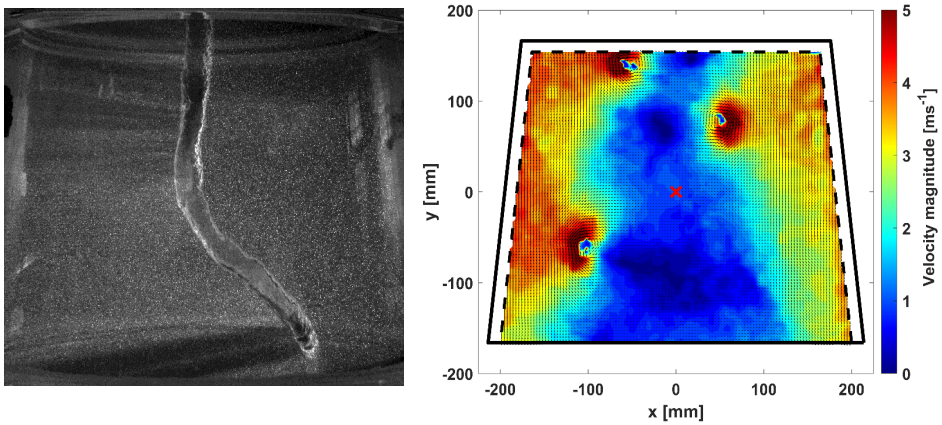


Figure 11: Left, PIV image with fluorescent particles and cavitation vortex rope, right, a velocity field example obtained from PIV.

This image is illuminated with a 200-mJ Nd:YAG pulsed laser. By installing an orange filter in front of the camera, the unwanted reflections from the cavity surface are eliminated and only the reflected light from the particles hits the sensor. To calculate the velocity field from the acquired images, each image is first de-warped; meaning that it is compared with a calibrated image of the same view, and thereby, each pixel is assigned with the physical coordinates. In the next step, a mask is applied to the images to remove the out-of-interest regions. The final step is to apply the cross-correlation PIV algorithm to

each two successive images to find the instantaneous velocity field. Ultimately, the instantaneous velocity fields obtained for a specific operating condition are (phase-) averaged over all the measured instants. Further analysis such as vortex center detection, determination of the precession radius, extraction of the vortex intensity and viscous core radius could be applied to the obtained velocity fields to get more quantitative information from the flow.

# 4 Results and discussion

## 4.1 Frequency response

**Measurements on PF1 (first experimental campaign)**

The eigen frequencies computed by the modal analysis on the pressure measurements at the different locations along the pipes of the PF1 test rig are shown in Figure 12. In particular, the first eigen frequency of the system is presented as a function of the discharge factor.

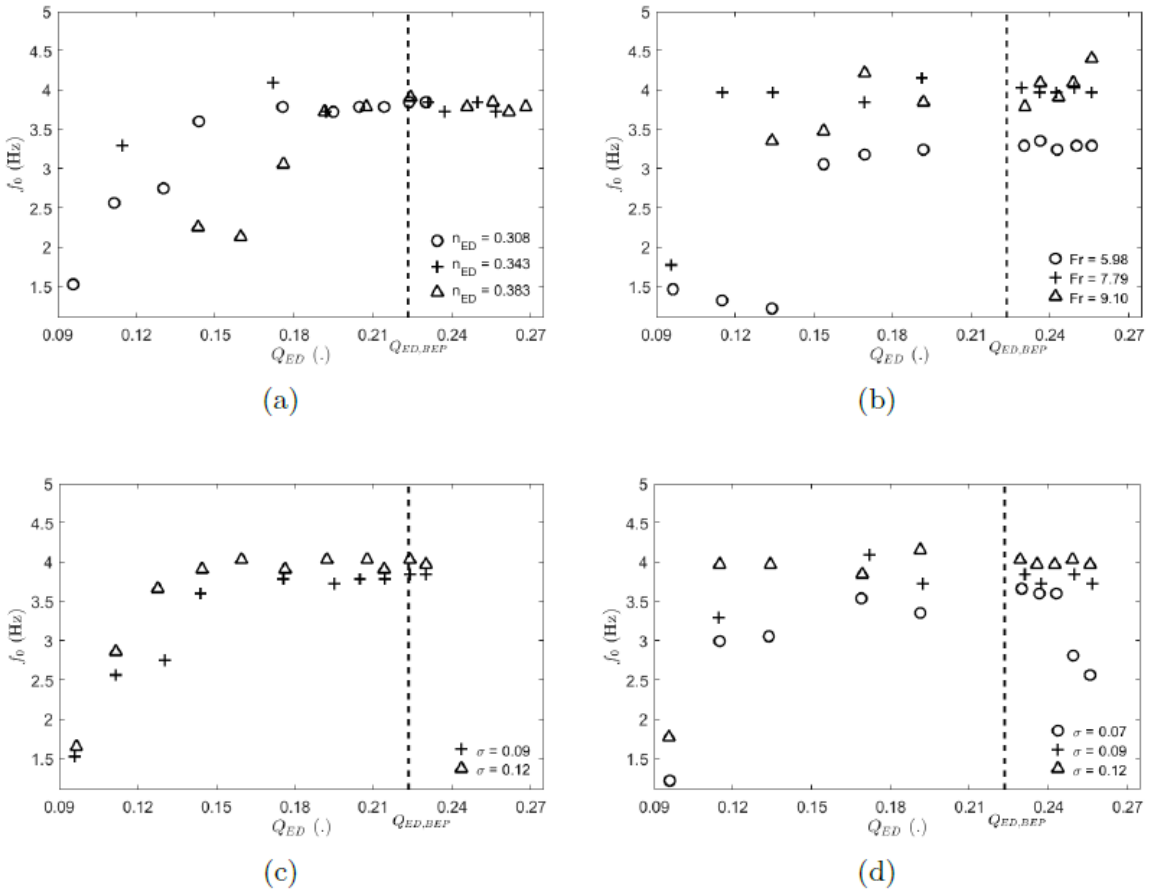


Figure 12: Influence of discharge factor on first eigen frequency $f_0$ of system, for different speed factors at $Fr = 7.79$ and $\sigma = 0.09$ (a), different Froude numbers at $n_{ED} = 0.343$ and $\sigma = 0.12$ (b), different Thoma numbers at $Fr = 7.79$ and $n_{ED} = 0.308$ (c) and at $Fr = 7.79$ and $n_{ED} = 0.343$ (d).

This clearly highlights the influence of the speed factor, Froude number and Thoma number as follows:

- At part load, the natural frequency increases with a growing discharge factor until a maximum value close to the BEP. At full-load stable conditions, it seems to be constant while it decreases at unstable full-load conditions.
- The speed factor has a greater influence at low discharge factors where the natural frequency is lower for higher speed factors.
- The natural frequency increases with the Froude number and the Thoma number.

Similar trends could be observed for the second eigen frequency of the system as a function of the same parameters as for the first eigen frequency.

## Measurements on PF3 (second experimental campaign)

The results of the modal analyses of the full-load conditions performed on PF3 are presented here. In Figure 13, the evolutions of $f_0$ with respect to $\sigma$ and the unit discharge factor $Q_{ED}$ are shown. Excluding some probably erroneous values, i.e. $Q_{ED} = 0.272$ at $\sigma = 0.06$ and $Q_{ED} = 0.256$ at $\sigma = 0.08$ for $n_{ED} = 0.357$, three common trends are detectable. Indeed, an increase in $f_0$ may be associated with a rise in $\sigma$, a decrease in $Q_{ED}$ and an increase in $n_{ED}$. The identified $f_0$ increases when a decrease in the cavitation volume occurs. In addition, it is interesting to observe how for the lower unit speed factors $n_{ED} = 0.293$ and $n_{ED} = 0.325$, the slope of the $f_0(\sigma)$ curves tends to remain almost constant on the entire $\sigma$ range, while for higher unit speed factors $n_{ED} = 0.343$ and $n_{ED} = 0.357$ a decrease in this slope for the higher pressure levels is remarkable.

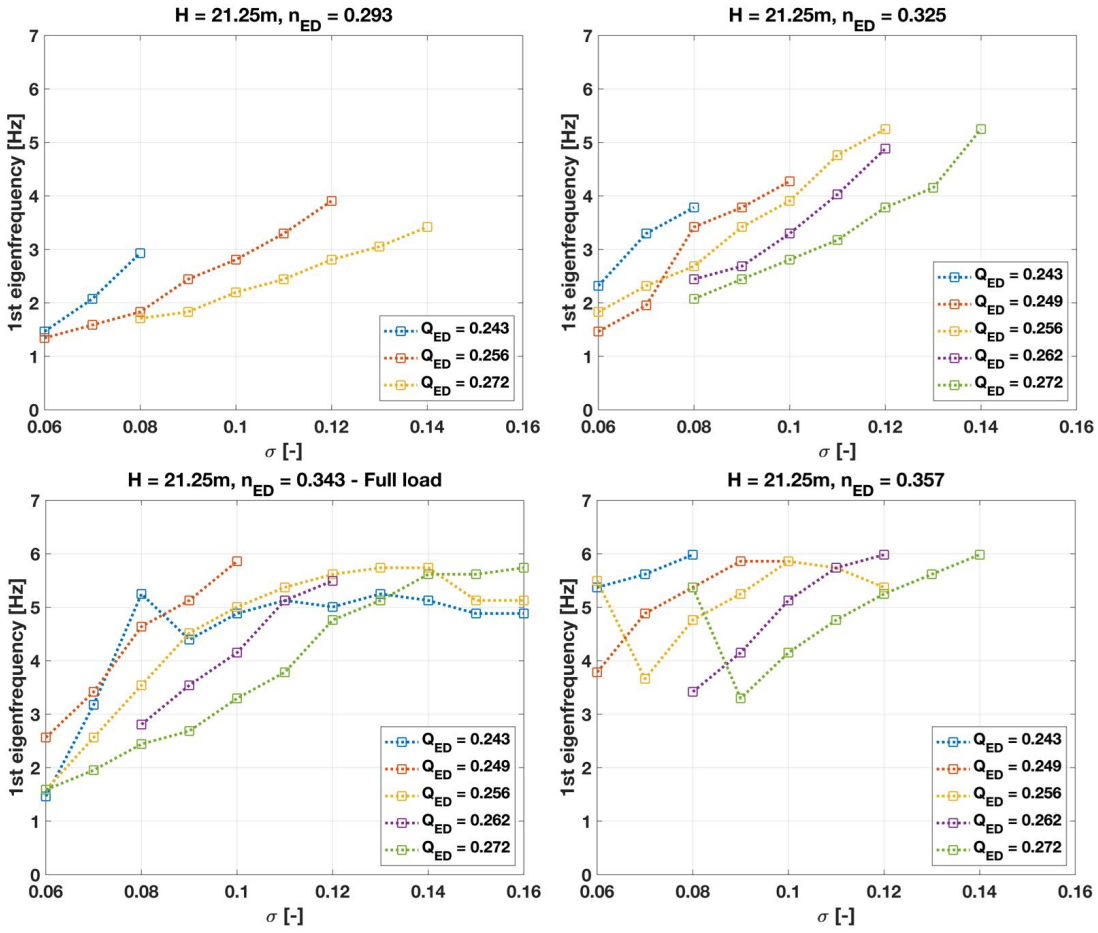


Figure 13: Evolution of $f_0$ with $n_{ED}$, $Q_{ED}$ and $\sigma$.

In the following, the details of the analysis for one speed factor and one discharge factor are presented. The studied case is the turbine operating condition defined by $H = 21.25$ m, $n_{11} = 0.343$ and $Q_{ED} = 0.272$. For this condition, the detected time domain response for every $\sigma$ value has been divided into a set of subintervals, on each of which a fast Fourier transform is applied. For time intervals small enough, they are assumed to correspond to an almost constant excitation frequency $f_{exc}$ exerted by the excitation system. The wall pressure measurements of sensor #1 and #2 are considered. A cross-spectral density analysis is performed on each time interval and the results are shown in Figure 14. The colormaps present the intensity of the harmonic response as a function of the excitation frequency $f_{exc}$ and the excited frequency $f_0$. The red spot marks the location of the most prominent peak.

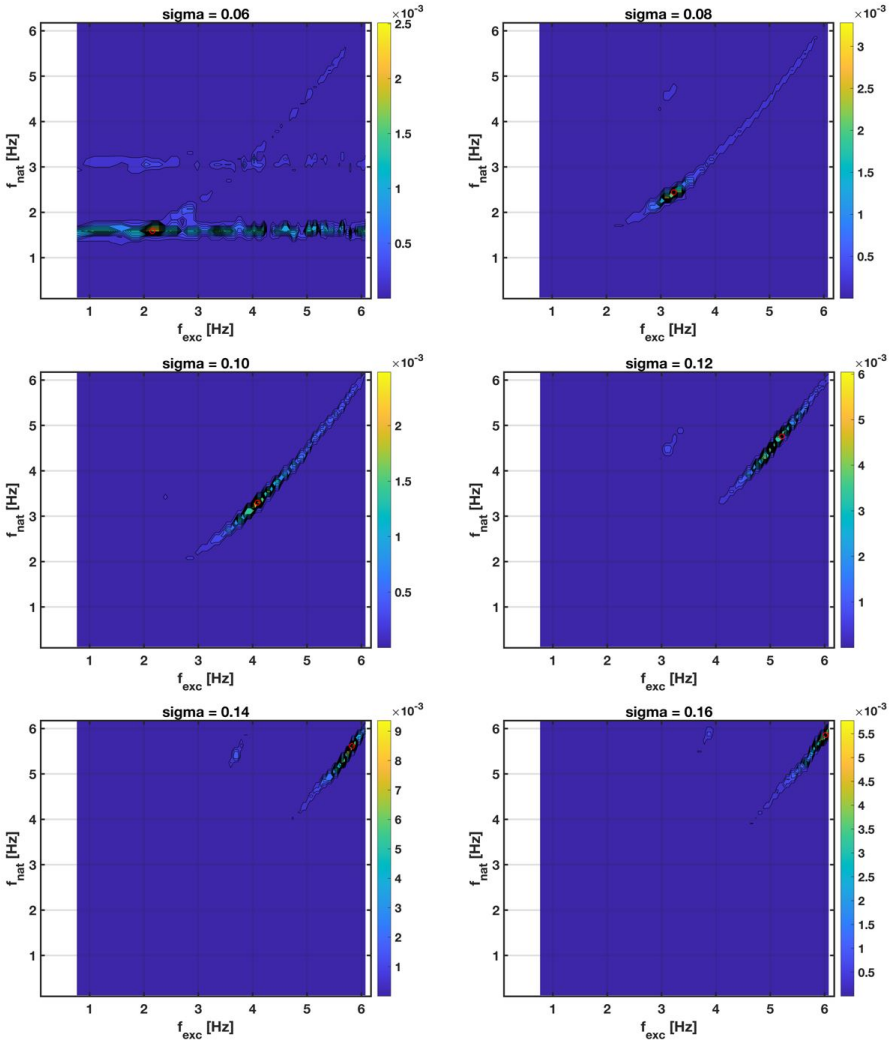


Figure 14: Cross-spectral density between pressure sensors #1 and #2 at $H = 21.25$ m, $n_{ED} = 0.343$ and $Q_{ED} = 0.272$.

A sequence of peaks located at a constant value of $f_0$ is visible in the first graph of Figure 14. The fact that these peaks are dominant for any value of $f_{exc}$ suggests that they are induced by an excitation source different from the excitation system. At $\sigma = 0.06$, a relatively large volume of cavitation forms in the draft tube, which may undergo an instability and lead to the full-load self-excited oscillations. For the others $\sigma$ values, the results are consistent and follow the same trend, for which $f_0$ increases with the Thoma number as the amount of cavitation volume decreases in the draft tube.

## 4.2 Precession frequency at part load condition

The precession frequency of the cavitation vortex rope can be observed by modal analysis of any sensor close to the turbine runner due to the pressure fluctuations in the draft tube cone caused by the vortex rope. The sensors in the draft tube cone have been chosen for this analysis, where the fluctuations are more pronounced. At low discharge factors, the vortex rope loses its periodicity and intensity. At higher values, however, the precession motion becomes quasi-axial. The results are shown in Figure 15. The precession frequency increases with the discharge coefficient until it reaches a maximum frequency before dropping to lower values. The speed factor and the Froude number tend to increase the precession frequency. In addition, the speed factor increases the developed regime of the cavitation vortex rope, which agrees with [3], and the maximum precession frequency is located at the higher speed factors. Finally, the Thoma number slightly reduces the maximum precession frequency with a stronger influence at the higher Froude number values. All these observations can be explained with the help of the speed triangle. By increasing the speed factor, the tangential velocity of the flow at the runner outlet is greater while the axial component remains constant for a fixed angle between the runner blade trailing edge and the relative flow velocity, thus increasing the swirl number. By increasing the Froude number and fixing the speed factor, the flow velocity at the outlet of the runner is greater and, therefore, its tangential component increases. Finally, by increasing the Thoma number, the cavitation volume is reduced, which decreases the vortex intensity and thus the tangential velocity of the flow.

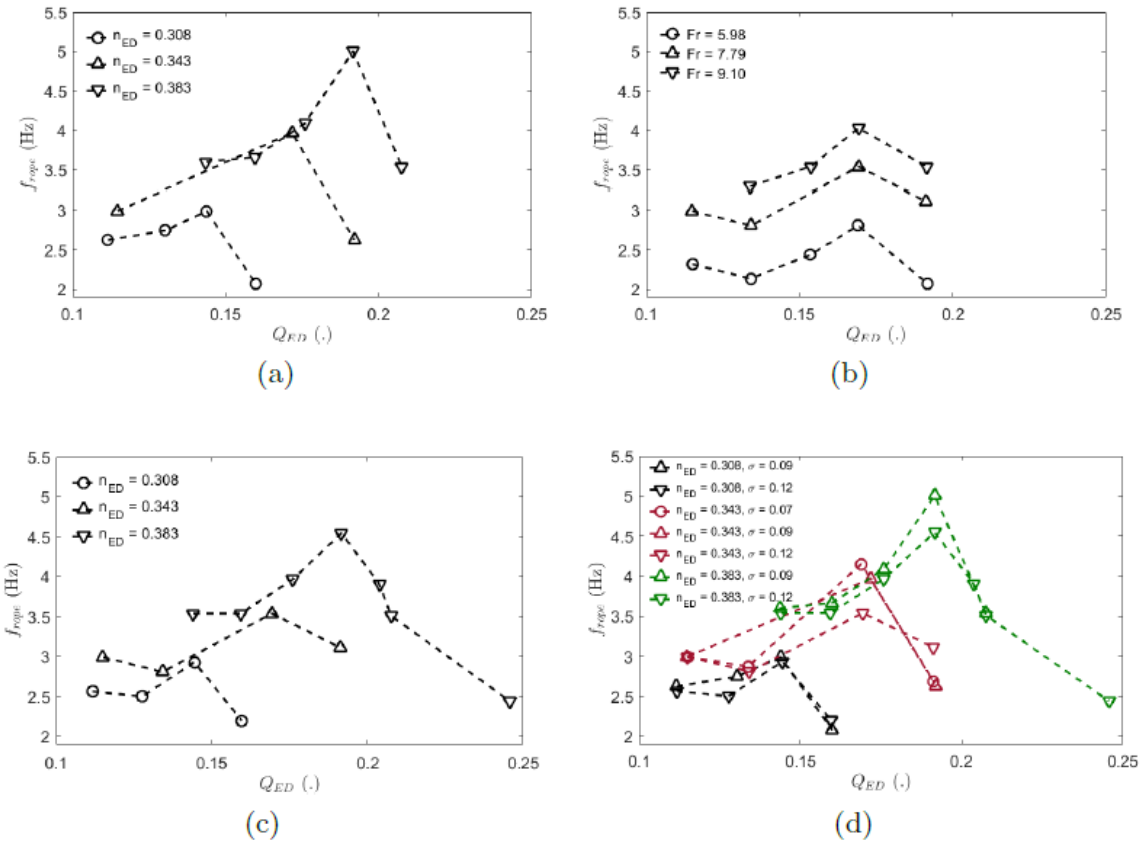


Figure 15: Influence of the discharge factor on the precession frequency of the vortex rope at: $Fr = 7.79$ and $\sigma = 0.09$ (a), $\sigma = 0.12$ (c), different Froude numbers at $n_{ED} = 0.343$ and $\sigma = 0.12$ (b), and different Thoma numbers (d).

## 4.3 Stability limits at full load condition

Experimental tests have been performed at different operating conditions by varying the discharge, the Thoma number, the Froude number and the rotational speed of the runner. For each test, the experimental procedure consists of four steps:

1. STEP 1: at constant discharge, the Thoma number is decreased to determine the limit of the unstable full-load operation, threshold 1 in Figure 16, which illustrates the time history of the pressure fluctuations in the draft tube cone.
2. STEP 2: the discharge is decreased until the system reaches back to the stable operation (threshold 2), while the Thoma number is kept constant.
3. STEP 3: the discharge is increased until its initial value at constant Thoma number by passing through the transition to the unstable condition (threshold 3) to evaluate the hysteresis of the instability threshold by changing the discharge.
4. STEP 4: the Thoma number is increased at constant discharge to return to the stable full-load condition (threshold 4) to evaluate the hysteresis of the instability threshold by changing the Thoma number.

The thresholds are determined by applying the histogram selection method to the pressure fluctuations signal in the draft tube cone, which identifies the pressure fluctuation peaks corresponding to the self-excited oscillation of the cavitation vortex rope. The stability limits as a function of the swirl number and the Thoma number are shown in Figure 17. It is noticed that for each speed factor, it is possible to identify the limit of the stable full-load operation as a function of the swirl number with a standard deviation equal to 15 % of the mean swirl number value, whatever the Froude number, the Thoma number and the discharge are. This interval on the swirl number value at the instability threshold is due to the influence of the Thoma number on the stability limit, which, therefore, should be also considered when predicting the stability limit. Furthermore, it is highlighted that it is possible to determine a linear increase in the swirl number value at the instability threshold depending on the Thoma number for different Froude number values.

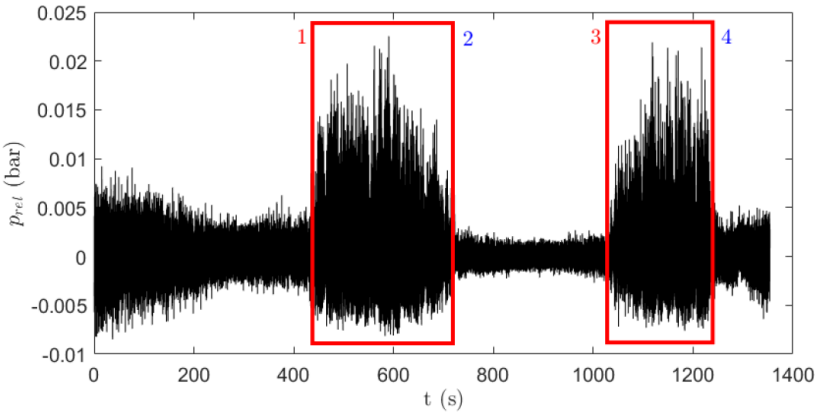


Figure 16: Time history of the pressure fluctuations in the draft tube cone for the operating point at $Fr = 8.5$ and $n_{ED} = 0.343$.

The analysis on the hysteresis of the stability limits of the full-load operation highlights that the maximum recorded hysteresis, when crossing the stability limit by decreasing the Thoma number, is 13.30 % of the Thoma number value at the threshold. This maximum hysteresis happens for the highest discharge factor. Results show that returning to the stable area requires a higher Thoma number. In addition, the hysteresis effect increases with the discharge while no significant trend is observed for the influence of Froude number and the speed coefficient. The results also suggest that the hysteresis of the instability

transition by increasing the discharge is limited, as the maximum deviation of the threshold is 1.94 % of the discharge factor. Furthermore, the study of the pressure fluctuations in the frequency domain has been performed to evaluate the effect of the operating condition on the frequency of the self-oscillation of the cavitation vortex rope. The results highlight that this oscillation occurs at the first eigen frequency of the hydraulic system during the unstable full load operation. The self-oscillation frequency is evaluated by computing the power spectrum of the pressure fluctuation signal divided in 5 % overlapping windows of 10s each, and by defining the targeted frequency as the one corresponding to an amplitude higher than 25 % of the peak amplitude over all the windows. This avoids low-amplitude peaks within the stable area and ensures that all the frequencies in the unstable area are considered. In Figure 18, the evolution of the self-oscillation frequency is illustrated as a function of the Thoma number and the discharge factor. It is observed that the first eigen frequency increases with the Thoma number at a fixed discharge, while it decreases as the discharge increases at a fixed Thoma number.

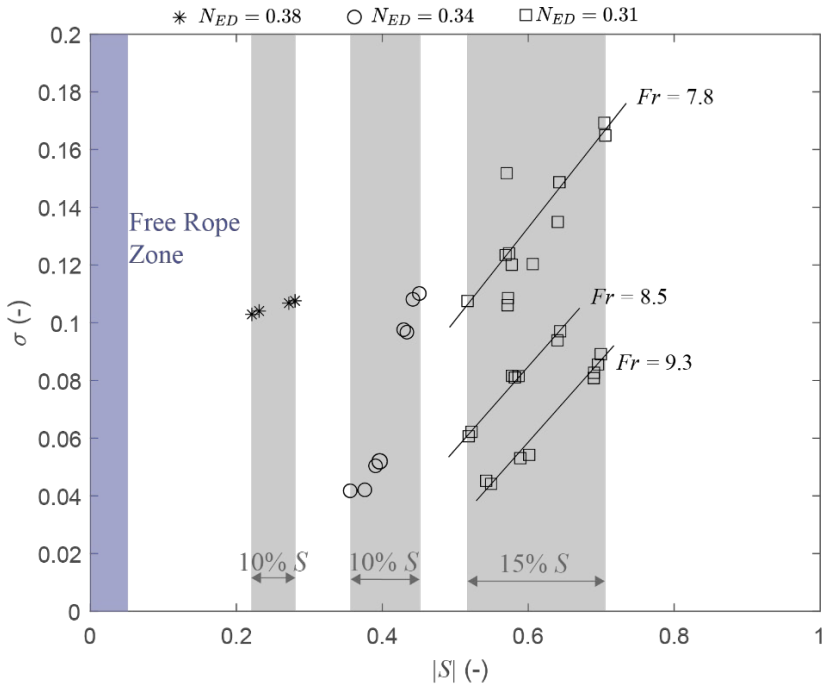


Figure 17: Stability limits as a function of the Thoma number and the swirl number defined by the measurements on the reduced-scale model.

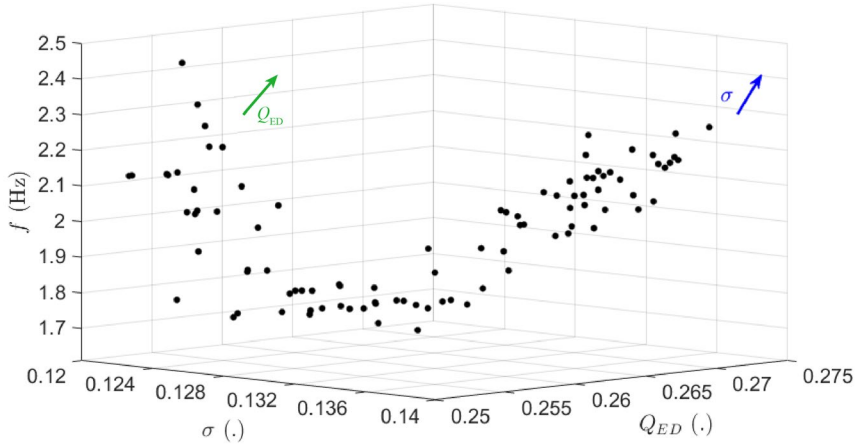


Figure 18: Evolution of the self-excited oscillation frequency of the pressure fluctuations in the draft tube cone as a function of the Thoma number and $Q_{ED}$ for the operating point at $Fr = 8.5$ and $n_{ED} = 0.343$.

## 4.4 Cavitation volume variations without external excitation

The time history of the cavitation volume of the vortex rope at full-load condition is presented for different discharge factors and constant Thoma number in Figure 19. The operating points with higher discharge have a greater cavitation volume. Volume fluctuations are observed for the higher discharge factors, which correspond to the self-excited full-load instability. The mean value of the cavitation vortex rope at full load condition is presented in Figure 20. Evidently, the value of the cavitation volume increases as the Thoma number decreases.

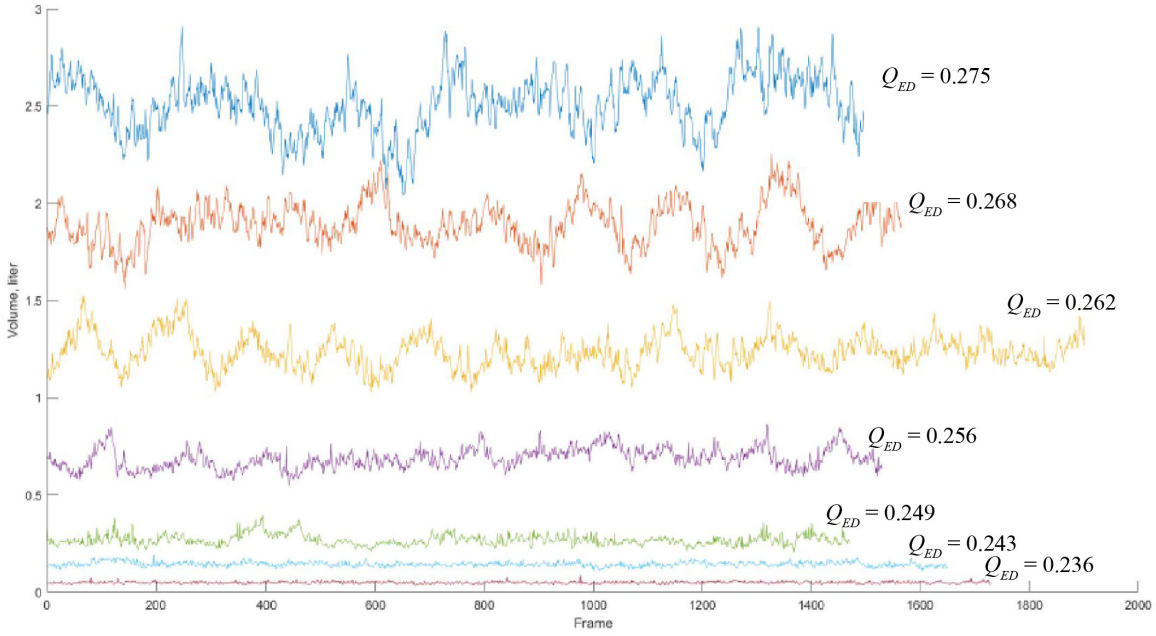


Figure 19: Time history of the cavitation volume estimated by image processing for different discharge coefficients and $\sigma = 0.09$.

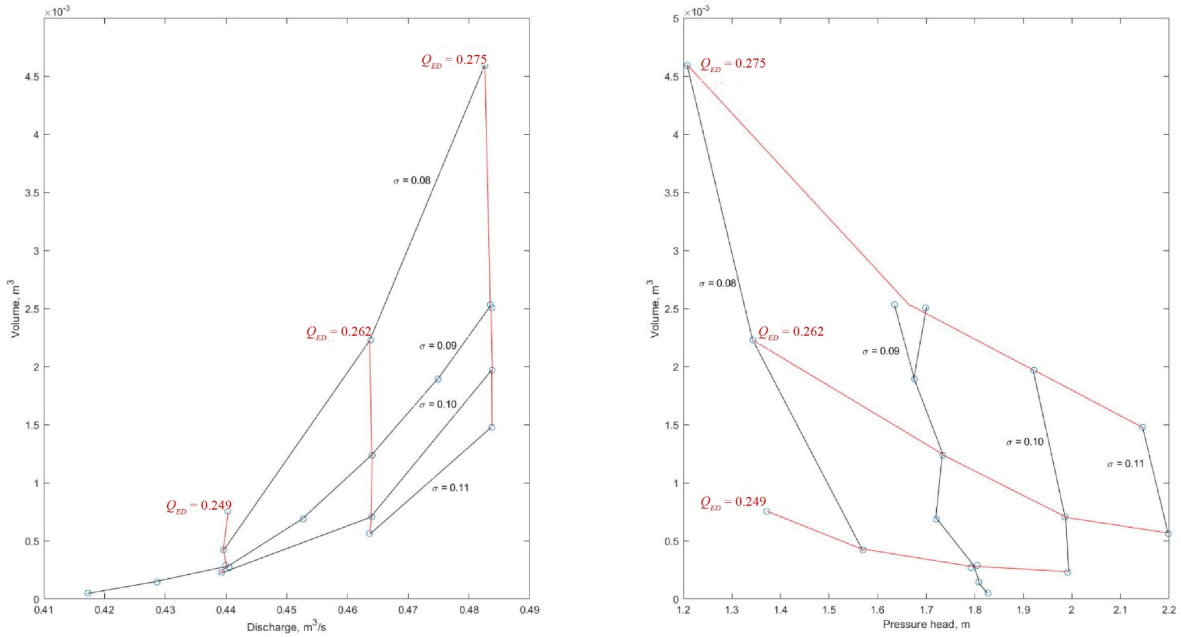


Figure 20: Average volume of the cavitation vortex rope as a function of the operating parameters of the machine.

The variations of the mean volume of the cavitation vortex are presented in Figure 21 as a function of the operating parameters including the speed factor, the discharge factor and the Thoma number. The most evident result observed is the decrease in the cavitation volume as the Thoma number increases. The unstable full-load cases could be recognized by the fact that at higher discharges, approaching the lower values of $\sigma$ results in a sudden increase of the slope for $V_c(\sigma)$ curves. Besides the dependency on $\sigma$, an influence of the discharge on the volume dimension is noticed. Moving away from the best efficiency point imposes an increase in the tangential component of the velocity triangle in the draft tube leading to a stronger swirling flow, and therefore, lower pressures developed. A decrease in volume is observed when the turbine speed factor increases at constant Froude number, discharge factor and $\sigma$. Such an increase in the speed factor results in a higher rotational velocity of the runner in the velocity triangle while the meridional component remains constant. This change results in a decrease in the swirl component in the draft tube, which, in turn, reduces the depression and the cavitation volume.

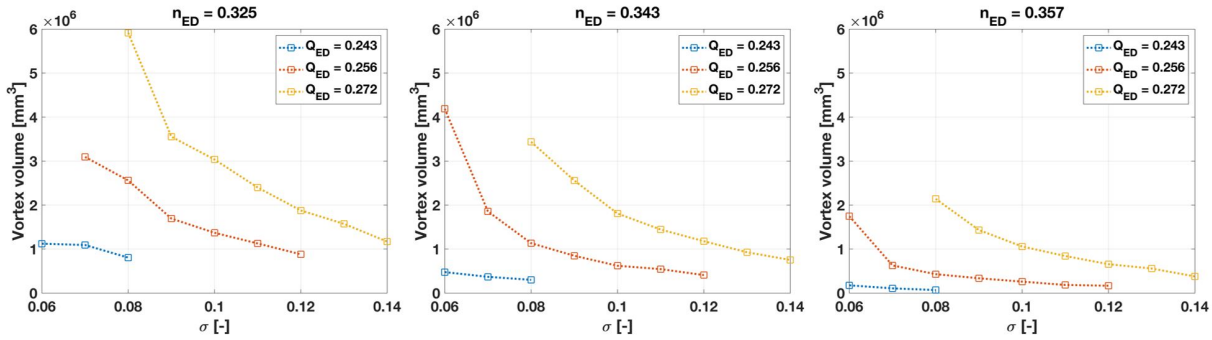


Figure 21: Dependence of $V_c$ on $n_{ED}$, $Q_{ED}$ and $\sigma$.

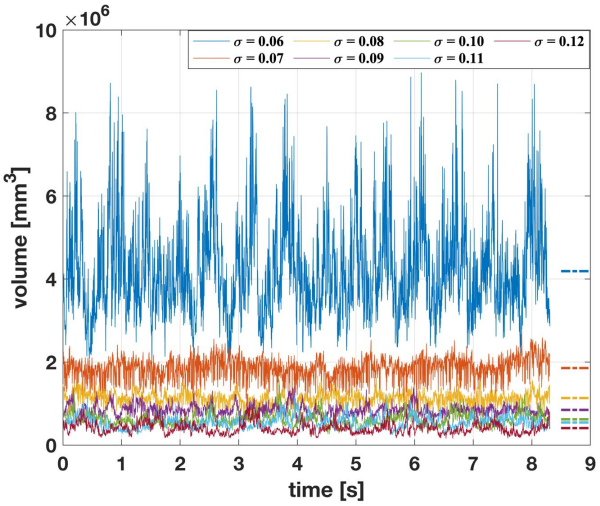


Figure 22: Time history of the cavitation volume as a function of $\sigma$ at $n_{ED} = 0.343$ and $Q_{ED} = 0.256$.

The unstable full-load conditions are characterized with a pulsating circular cavitation crown that forms at the draft tube cone inlet. This cavitation volume develops and collapses with a particular frequency inducing a self-excited oscillation, as explained by Müller [1]. To investigate the effect of the cavitation number on the behavior of the cavitation vortex rope at full-load conditions, the vortex volume evolution with time for seven different values of $\sigma$ is shown in Figure 22. The results presented in this graph correspond to $n_{ED} = 0.343$ and $Q_{ED} = 0.256$ operating conditions. The seven short line segments on the right side of the graph indicate the mean values for each Thoma number over the entire time evolution. As is clear, the high-amplitude self-excited oscillations start to appear at $\sigma = 0.09$.

For the operating point defined by $n_{ED} = 0.325$, $Q_{ED} = 0.272$ and $\sigma = 0.08$, the evolution of the cavitation volume of the vortex rope over one oscillation cycle is illustrated in Figure 23.

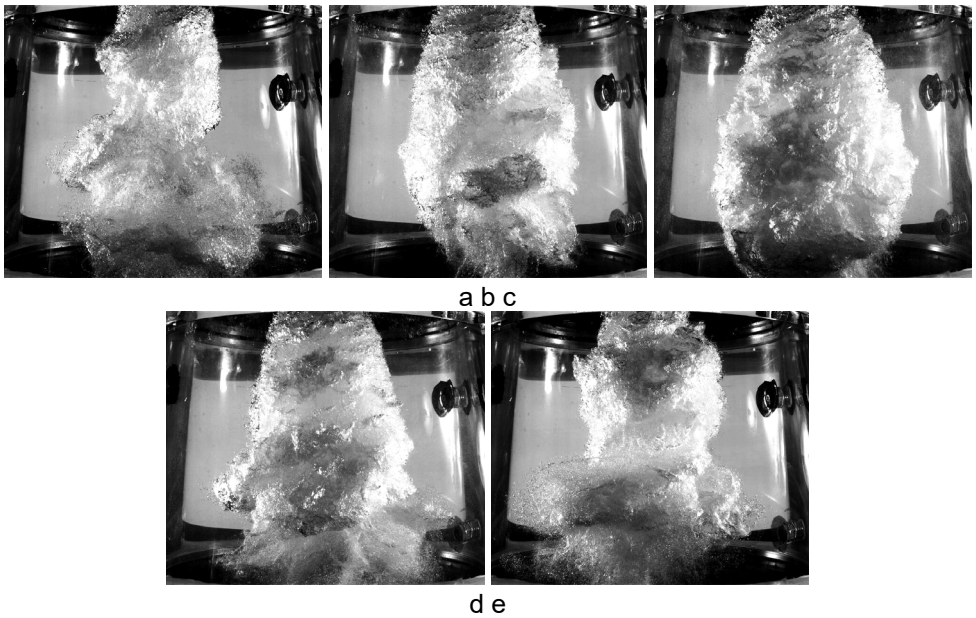


Figure 23: Vortex evolution during a periodic cycle at $n_{ED} = 0.325$, $Q_{ED} = 0.272$ and $\sigma = 0.08$.

For the same operating point, the evolution of the cavitation volume has been analyzed along with the synchronous pressure measurements at the draft tube wall. The cross-spectral density ( $CSD_{1,2}$ ) and the coherence ( $C_{1,2}$ ) of the two signals are computed via the following formula:

$$CSD_{1,2} = \frac{2dt}{N} F_1(\omega) F_2(\omega)^* \text{ and } C_{1,2} = \frac{|CSD_{1,2}|^2}{PSD_1.PSD_2} \tag{12}$$

where $dt$ is the sampling interval defined by $dt = 1/f_s$ (with $f_s$ being the sampling frequency), $T$ is the overall time period defined by $T = Ndt$ (with $N$ being the total number of samples), $F_1(\omega)$ is the Fourier transform of the first signal $f_1(t)$ and $F_2(\omega)^*$ is the complex conjugate of the Fourier transform of the second signal $f_2(t)$. $PSD$ stands for the power spectrum density of each signal and is calculated by:

$$PSD = \frac{2dt^2}{T}|F(\omega)|^2 = \frac{2dt}{N}|F(\omega)|^2 \tag{13}$$

The cross-spectral density and coherence of the cavitation volume and the pressure signals are plotted in Figure 24. It is clear from the two plots that the two mentioned signals oscillate in a synchronous manner in one dominant frequency (1.8 Hz), which is the first natural frequency of the circuit.

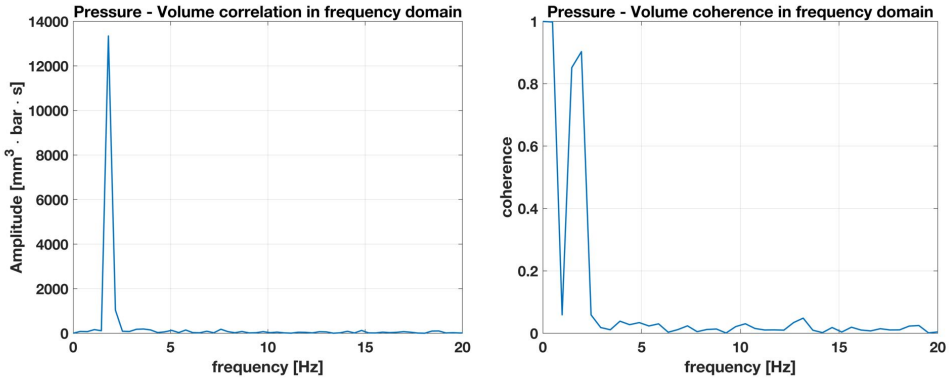


Figure 24: cross-spectral density and coherence of the volume and the pressure signals at $Q_{ED} = 0.272$ and $\sigma = 0.08$.

Performing a phase average on the pressure and volume signals in time, which are discretized in periods by the dominant frequency, allows visualizing the periodic cycle in a better way. The causal relation between the draft tube pressure and the cavitation volume is illustrated in Figure 25.

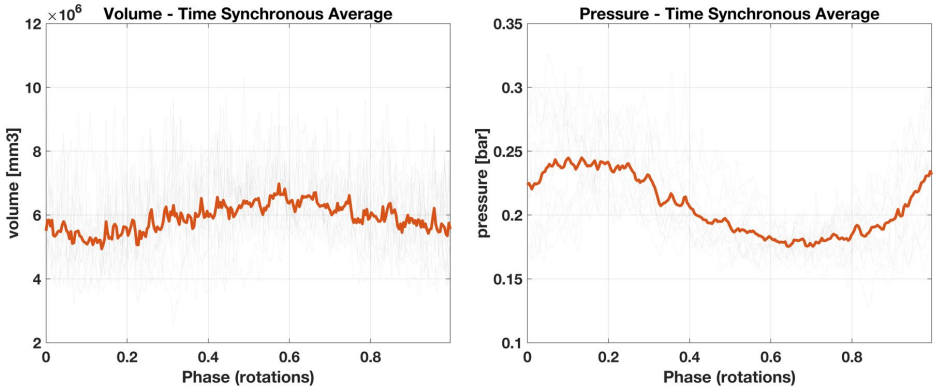


Figure 25: Phase-average draft tube pressure and cavitation volume signals at $n_{ED} = 0.325$, $Q_{ED} = 0.272$ and $\sigma = 0.08$.

The most dominant peaks resulting from a correlation analysis between the volume and pressure signals are shown in Figure 26 for every single operating condition.

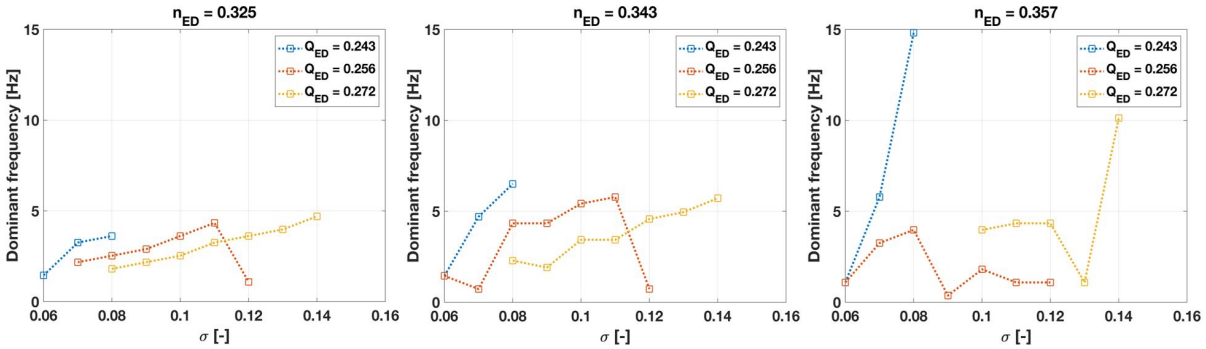


Figure 26: Evolution of full-load self-oscillation frequency with $Q_{ED}$, $n_{ED}$ and $\sigma$.

Three trends appear by evaluating the results. Namely, the dominant frequency increases if $n_{ED}$ is increased, $Q_{ED}$ is decreased, or $\sigma$ is increased. These three relations are consistent with the results obtained from the dynamic modal analysis. In fact, an increase of the cavitation volume (by any means) is associated with a drop in the hydraulic circuit natural frequency. Moreover, except for some cases where extremely low or high dominant frequencies are detected due to some possible errors in the analysis, every peak is in a range between 1 Hz and 6 Hz, which are reasonable boundaries for defining the upper and lower bonds of the test rig first natural frequency.

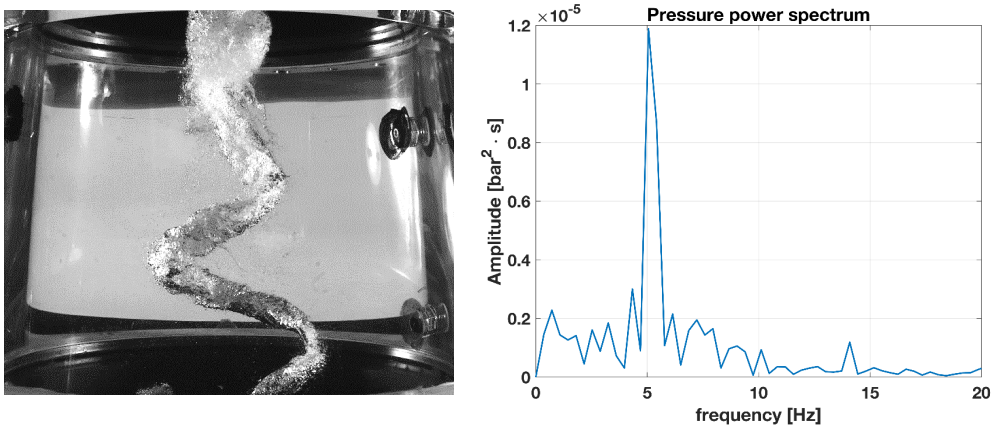


Figure 27: Helical vortex rope with precession motion at full load condition: $n_{ED} = 0.343$, $Q_{ED} = 0.256$, $\sigma = 0.10$.

An interesting and peculiar observation was made during the full load experiments on this model test. Although the full load is characterized by the formation of a relatively large cavitation structure attached to the turbine hub, which may undergo self-excited oscillations and induce full load instability, in case of this specific Francis turbine, the vortex rope gets a helical shape and experiences a precession motion. This phenomenon is clearly depicted in Figure 27 (left). This behavior, which is like the part-load flow patterns, results in fluctuating pressures in the draft tube at the precession frequency. These fluctuations, which generate a distinct peak in the frequency domain Figure 27 (right), may lead to the structural vibrations if they coincide with the hydraulic circuit natural frequencies. This unexpected behavior requires further investigations to be explained.

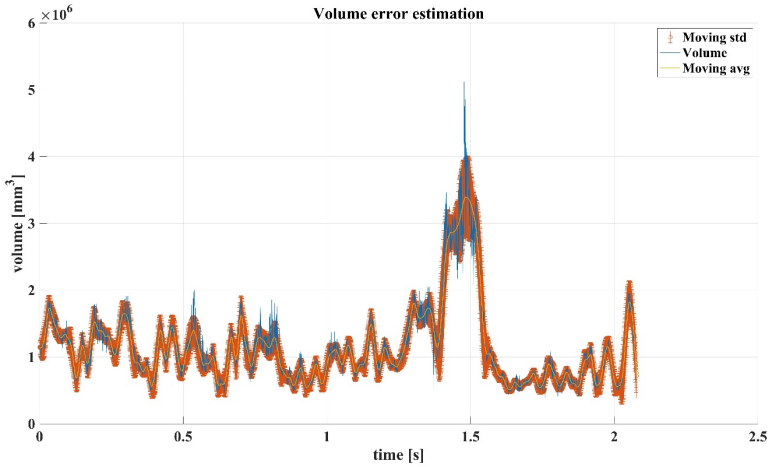


Figure 28: time evolution of the cavitation volume for $n_{ED} = 0.343$, $Q_{ED} = 0.185$ and $\sigma = 0.06$.

The time history evolution of the cavitation volume within the vortex rope at part-load conditions is depicted in Figure 28. The analyzed video corresponds to the operating point at $H = 21.25$ m, $n_{ED} = 0.343$, $Q_{ED} = 0.185$ and $\sigma = 0.06$. It should be noted that this operating point suffers from the so-called ‘‘upper part-load instability’’, which is associated with an elliptical cross section of the vortex rope at self-rotation. This leads to some additional fluctuations in the detected volume due to the periodic exposure of the larger and smaller diameters of the ellipse to the camera. Another interesting point is the vortex behavior captured in the time range between 1.2 s and 1.6 s, i.e. a sudden increase in the volume followed by a quick decrease. This behavior corresponds to a vortex breakdown followed by a collapse. This sequence is well depicted in Figure 29. Once the vortex breakdown is initiated, the cavitation vortex rope is twisted in the middle of the draft tube cone leading to an accumulated cavitation volume. This event is followed by a collapse of the cavity due to the pressure rise induced by the breakdown. At this point, the vortex takes the original cylindrical shape and the cycle restarts.

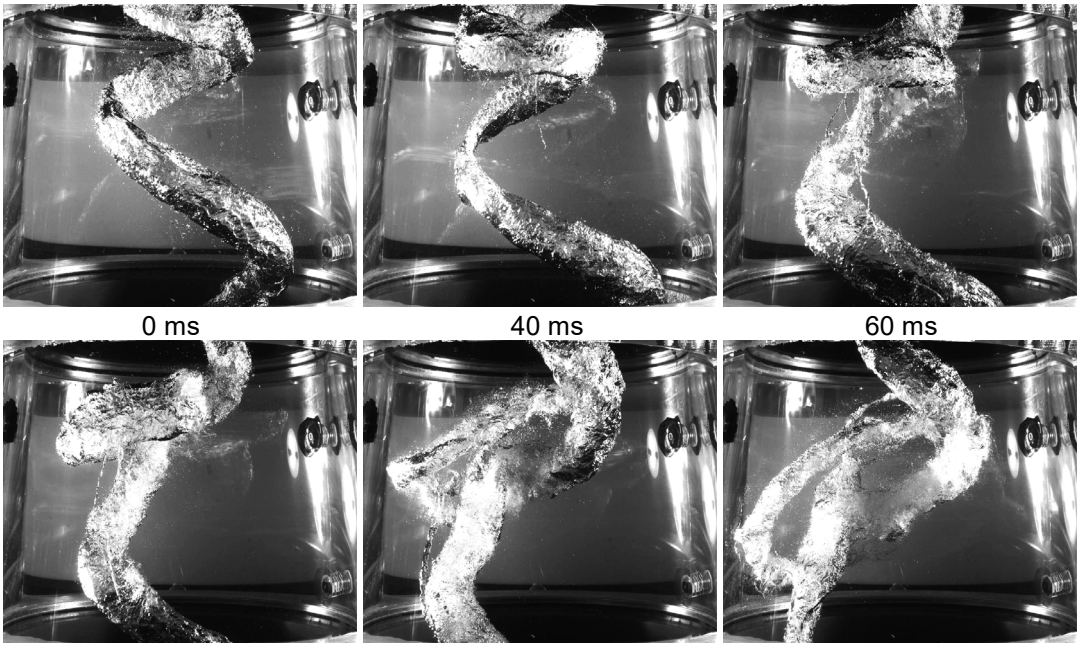

190 ms 220 ms 250 ms

Figure 29: vortex breakdown, collapse, and re-establishment at $n_{ED} = 0.343$, $Q_{ED} = 0.185$ and $\sigma = 0.06$.

## 4.5 Cavitation volume variations with external excitation

Measurement of the pressure fluctuations and flow visualizations with excitation system at one operating point at full load are performed to study the effect of the excitation at the system first and second eigen frequencies on the stability of the vortex rope. For each frequency, different pump rotational speeds are tested to investigate the effect of the excitation amplitude on both the dynamic response of the test rig and the fluctuations of the cavitation volume in the draft tube. The influence of the excitation amplitude on the amplitude and phase of the response of the test rig when excited at its first and second eigen frequencies is given in Figure 30 and Figure 31, respectively. The distribution of phase along the test rig is not modified when the amplitude of the excitation is increased, while the amplitude of the response increases as expected. It is demonstrated that the cavitation volume and the pressure are more likely to oscillate at the first eigen frequency of the circuit, as highlighted in Figure 32. Without the excitation system, the system is stable at this operating condition. Furthermore, the amplitude of both the cavitation volume and pressure fluctuations in the draft tube seems to reach a limit value when the amplitude of the excitation discharge is increased. As the excitation amplitude increases, a phase shift between both quantities appears and tends to the value observed at an unstable full-load operating point.

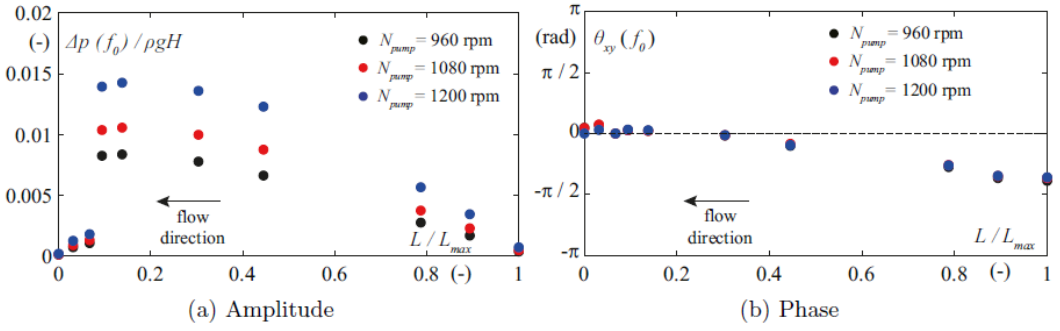


Figure 30: Amplitude and phase of the test rig response when excited at its first eigen frequency with different flow excitation amplitudes.

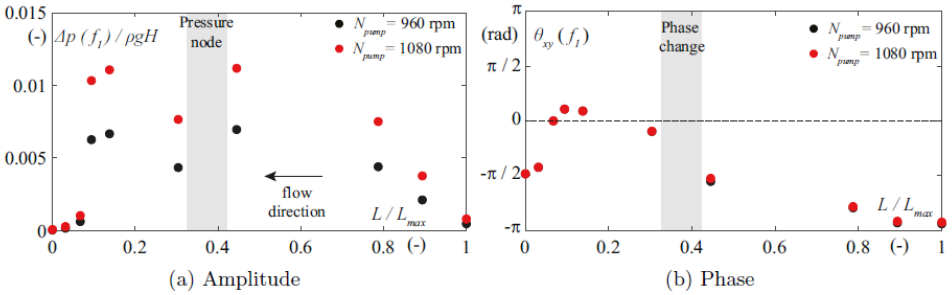


Figure 31: Amplitude and phase of the test rig response when excited at its second eigen frequency with different excitation amplitudes.

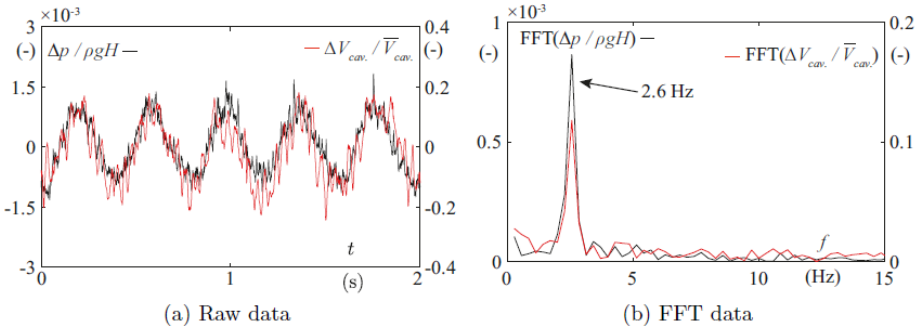


Figure 32: Time history of the pressure and cavitation volume in the draft tube (a) and corresponding FFT (b) when the test rig is excited at the first eigen frequency with $N_{pump}$ = 690 rpm .

## 4.6 1-D Numerical simulation of PF1

Pressure measurements and the estimation of the cavitation vortex rope enable the calculation of the hydro-acoustic parameters of interest to perform 1-D numerical simulations on the machine installed on PF1. As the cavitation volume of the vortex rope could be computed, Method 2 is applied. Furthermore, the tested operating conditions were not enough to compute the regression of the non-dimensional wave speed, which is necessary to apply Method 1 for the calculation of all the hydro-acoustic parameters.

In the calculation of the bulk viscosity, it has been noticed that the theoretical equation given in Eq. (8) does not provide an accurate representation of this hydro-acoustic parameter for this machine. The computed value of the bulk viscosity would lead to a computed eigen frequency significantly higher than the measured one. Therefore, a constant value has been assumed and further investigation are ongoing to correctly predict this parameter. However, even by fixing a constant value for the bulk viscosity, a good agreement with the eigen frequency resulting from the experimental measurements is found (within ±5 % of the measured eigen frequency).

## 4.7 1-D Numerical simulation of PF3 to predict the natural frequency values

The prediction of the eigen frequency values of the PF3 is performed by 1-D numerical simulations of the PF3 SIMSEN model and by considering the hydro-acoustic parameters computed for the PF1 thanks to the results of the first experimental campaign. This is performed in MATLAB® environment that runs SIMSEN at the desired operating point and computes the respective eigen frequency. The code is based on a stabilization of the SIMSEN model at the right head and discharge followed by the computation of the eigenvalues of the evolution matrix of the system. Finally, the stability of each operating point is

assessed through the evaluation of the real and imaginary parts of the first few eigenvalues. This procedure is carried out for each operating point.

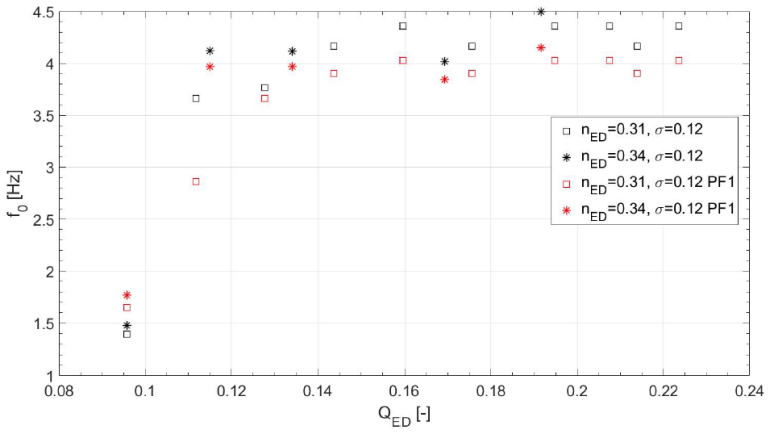


Figure 33: First eigen frequencies at part load computed by the SIMSEN model of the PF3 and their equivalent frequencies measured on the PF1 at part load.

To achieve this goal, the SIMSEN model is first stabilized at the desired discharge. For this purpose, SIMSEN is run with the corresponding input parameters, namely the valve opening and the pump and the turbine speeds found during the operating point measurement. For each operating point, the following parameters are also updated in the SIMSEN model before the initialization: the wave speed in the draft tube cone, the mass flow gain factor and the pipe viscosity, which have been deduced from the modal analysis of the experimental results of the first experimental campaign on the PF1. The computed eigen frequencies by the numerical simulations are presented in Figure 33 for the part-load conditions and in Figure 34 for the full-load conditions. It can be observed that the natural frequencies predicted for the PF3 are slightly higher than the natural frequencies measured for the PF1 at the same operating condition of the Francis turbine.

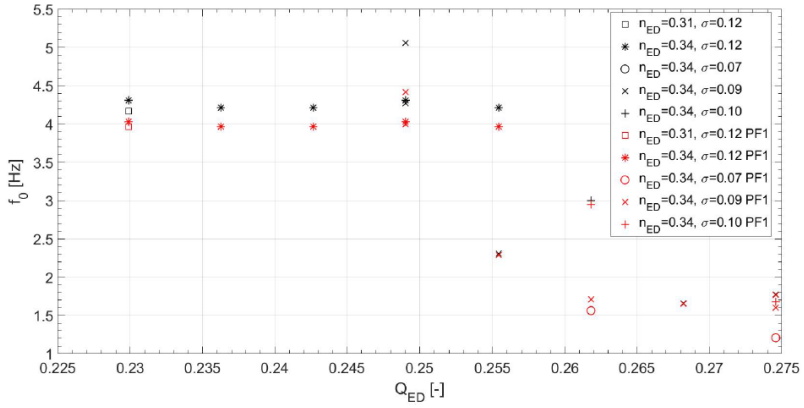


Figure 34: First eigen frequencies at full load computed by the SIMSEN model of the PF3 and their equivalent frequencies measured on the PF1 at full load.

## 4.8 Calculation of the hydro-acoustic parameters (volume-based method)

The first hydro-acoustic parameter that is computed is the mass flow gain factor $\chi$, which indicates the variation of the cavitation volume $V_c$ as a function of the variation of the discharge $Q$. The obtained results for the various operating conditions are shown in Figure 35. It should be noted that each $\chi$ value

is attributed to two values of the discharge coefficient, based on which the derivative (definition of the mass flow gain factor) has been calculated. The red dots in the plots, however, represents the $\chi$ value that is simply the average of the two other values obtained for that specific Thoma number at each $n_{ED}$. In general, the absolute value of $\chi$ increases for a decreasing $\sigma$. At full-load conditions, this behavior plays an important role in initiating the unstable self-excited regime. This means that at full load, for very low $\sigma$ value, a slight increase in the discharge may induce a large rise in the cavitation volume. This is exactly the mechanism that limits the maximal power provided by the machine at full-load conditions. A small increase in the discharge may cause a rapid growth of the cavitation volume leading to the development of the full load instability. This is coherent with the rise in absolute value of $\chi$ for higher $Q_{ED}$. The same reasoning applies with the speed factor: the higher $n_{ED}$ is, the higher must be the discharge to generate a certain cavitation volume. This is, therefore, coherent with a decrease in $\chi$ for an increase of $n_{ED}$.

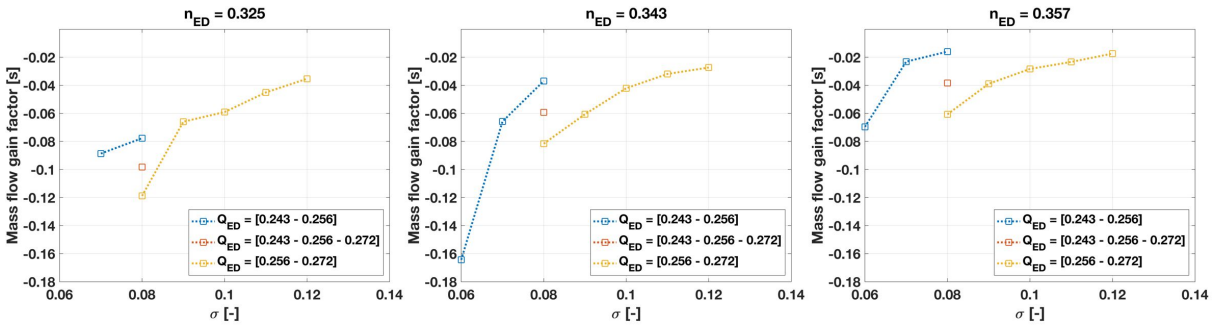


Figure 35: Evolution of $\chi$ with $n_{ED}$, $Q_{ED}$ and $\sigma$.

The behavior of the wave speed is shown in Figure 36. The general trend seems to be coherent. An increase in the wave speed requires a decrease in the cavitation volume as the gaseous phase provides an additional compressibility term, which acts in an inversely proportional way with respect to the system stiffness and the wave speed. At full-load condition, an increase in wave speed is, therefore, achieved by an increase in $\sigma$, a decrease in $Q_{ED}$ or an increase in $n_{ED}$, as shown in the plots. The numerical values obtained for the wave speed, which lie between 10 m/s and 60 m/s, are coherent with the typical values found in most of the cited references.

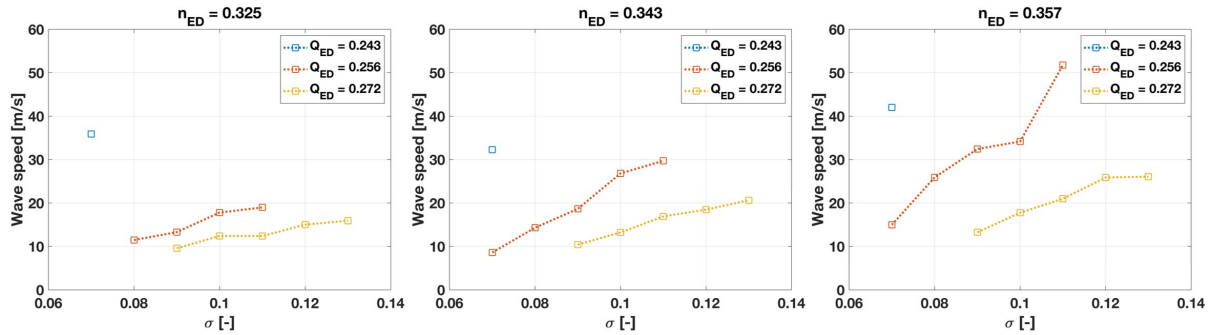


Figure 36: Evolution of $a$ with $n_{ED}$, $Q_{ED}$ and $\sigma$.

The computation of the bulk viscosity $\mu''$ is performed based on the dimensionless wave speed $\Pi$ values (refer to Eq. (4)). The computation of the bulk viscosity is, however, associated with high uncertainties. This is partly since the relation established by Landry et al. in [5] linking $\Pi$ and $M''$ has not been confirmed to be general for all the Francis turbines. The second reason is he square relation between $M''$ and $\Pi$, which means that the computed bulk viscosity depends on $a^4$, the fourth power of $a$. Thus, a slight error in the wave speed computation results in an amplified error for the bulk viscosity.

The values of the computed bulk viscosities are shown in Figure 37, where the trends followed by $\mu''$ with respect to other parameters are consistent with Landry et al. work [5]. Knowing that a decrease in the cavitation volume induces a rise in the bulk viscosity, it is coherently observed that an increase in $\mu''$ is caused by an increase in $\sigma$, a decrease in $Q_{ED}$ or an increase in $n_{ED}$.

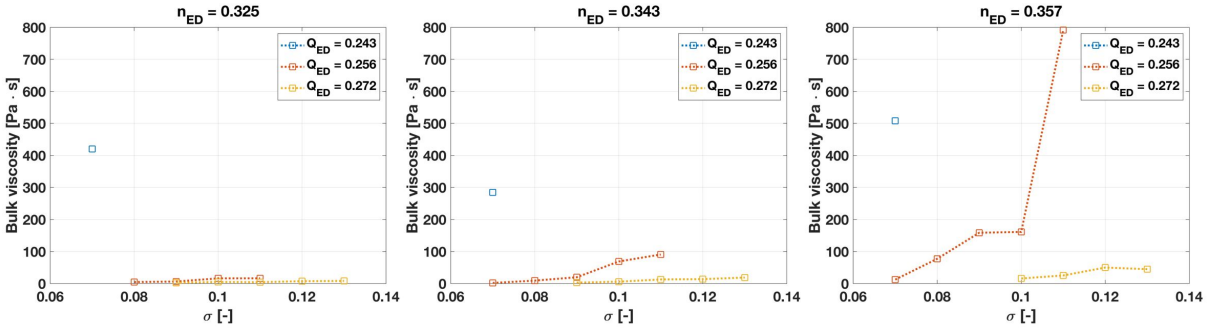


Figure 37: Evolution of $\mu''$ with $n_{ED}$, $Q_{ED}$ and $\sigma$.

## 4.9 PIV measurements and flow instabilities

As described earlier, PIV measurements have been used to identify the instability sources in the draft tube both at part load and at full load conditions. To be concise, only the results obtained for the upper part-load instability are presented here. It is known that the frequency of the part-load precessing vortex rope ($f_{rope}$) corresponds to 0.2 to 0.4 of the runner rotational frequency. Particularly, in the higher part-load operation range, i.e. 70% to 85% of the nominal discharge, this vortex might be accompanied by large-amplitude pressure fluctuations with a distinct frequency peak ($f_{upper}$) in the range of 2–4 times the runner rotational frequency [14], [15] and [16]. The onset of this instability leads to severe vibrations in the hydraulic circuit, which affects the performance of the machine. This upper part-load instability is usually associated with an elliptical-shaped vortex rope. Koutnik et al. [17] and Kirschner et al. [18] attribute the high-frequency pulsations to the self-rotation of the elliptical vortex rope, which develops an asymmetrical pressure distribution around itself. In addition to the self-rotation, Nicolet et al. [16] also bring up the possibility of a breathing pattern in the time history of the cavitation volume.

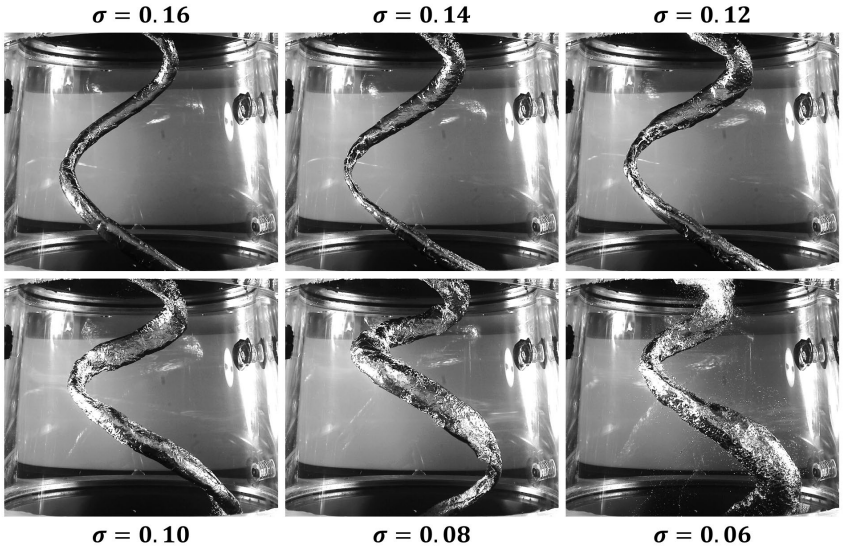


Figure 38: Effect of cavitation number on the state of the cavitation vortex rope at $n_{ED} = 0.343$ and $Q_{ED} = 0.185$.

The effect of reducing $\sigma$ on the state of the cavitation vortex rope is illustrated in Figure 38. The results correspond to an operating point with nominal head and rotational speed and $Q_{ED} / Q_{ED,BEP} = 0.84$. At the higher cavitation number, the vortex rope possesses a circular shape. It is enough to slightly reduce the cavitation number ($\sigma = 0.14$) to initiate the instability. At this $\sigma$, the vortex rope cross section takes an elliptical shape and generates high-amplitudes noise at frequency values higher than $f_{rope}$. This trend continues as the cavitation number is further reduced. At the lower values of $\sigma$ (i.e. 0.08 and 0.06), the vortex rope loses its coherent shape and shows chaotic behavior with intermittent collapses and recoveries.

The variation of the cone pressure is shown in Figure 39 (left), which is measured at position $p_1$ over a period of 1 s for the same flow condition and cavitation numbers as in Figure 38. As is clear, at $\sigma = 0.16$, the upper part-load instability is not yet activated and the pressure signal corresponds to the periodic passage of the vortex by the sensor position. However, at $\sigma = 0.14$, the pressure signal presents a different pattern and has a much richer content. As the instability initiates at this point, high-amplitude oscillations at $f_{upper}$ modulate with the precession frequency. The measured signals at $\sigma = 0.12$ and $0.10$ are very similar to that of $\sigma = 0.14$. However, at the lower values of the cavitation number, the vortex starts to lose its coherent shape due to the increased amount of cavitation in the cone, and consequently, the modulation is undermined. The power spectrum of the measured pressure signals for the same flow conditions is illustrated in Figure 39 (right). The peaks that are closely placed at around 4 Hz and 8 Hz correspond to $f_{rope}$ and its first harmonic. At the higher value of $\sigma = 0.16$, no other distinct peaks are observed. However, the initiation of the instability at $\sigma = 0.14$ is associated with the appearance of an outstanding peak at about 48 Hz. As the cavitation number is reduced to 0.12 and 0.10, $f_{upper}$ decreases constantly while the magnitude of the peak increases considerably. At lower values of cavitation number, $f_{upper}$ continues to decrease further, however, the amplitude of the fluctuations at $f_{upper}$ reduces drastically. A deeper look at the plot reveals the existence of side peaks next to the higher frequency peaks at $f_{upper} \pm f_{rope}$, which is in line with the previous studies [17], [19]. It is believed that the occurrence and development of the upper part-load instability depends strongly on the cavitation volume in the draft tube. For the higher values of $\sigma$, the amount of cavitation is not enough to lead to such high-amplitude oscillations. Depending on the operating condition, there might be a critical cavitation number, for which the circular vortex turns into an elliptical shape. This gives rise to pressure fluctuations at $f_{upper}$, most probably due to the self-rotation of the vortex. Once the instability is initiated, a further increase in the cavitation volume increases the compressibility of the flow and leads to higher-amplitude pressure fluctuations.

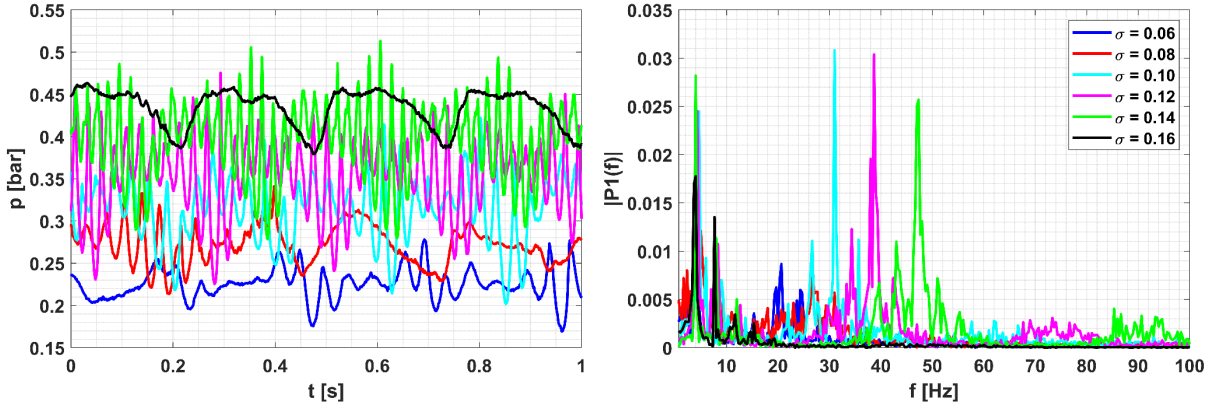


Figure 39: Effect of cavitation number on pressure variations in the draft tube and its frequency content at $Q_{ED} = 0.185$.

PIV measurements were performed for the nominal conditions in terms of head and rotational velocity and for a slightly lower discharge value ($Q_{ED} / Q_{ED,BEP} = 0.80$) compared to the previous results, to limit

the amount of cavitation it the draft tube and ensure an optimal visual access to the measurement planes. The variation of the draft tube pressure is depicted in Figure 40, in which the pressure is measured at the locations of the upper ($p_5$) and lower ($p_6$) laser planes for the non-cavitation precessing vortex (left) and the cavitation vortex rope with the upper part-load instability initiated (right). These pressure signals have been phase-averaged on the precession cycle based on the min-to-min location over 1000 s of PIV acquisition for each operating point. As it is clear in Figure 40, the activation of the upper part-load instability leads to inter-period fluctuations within the main precession cycle and increases the standard deviation of the signals significantly.

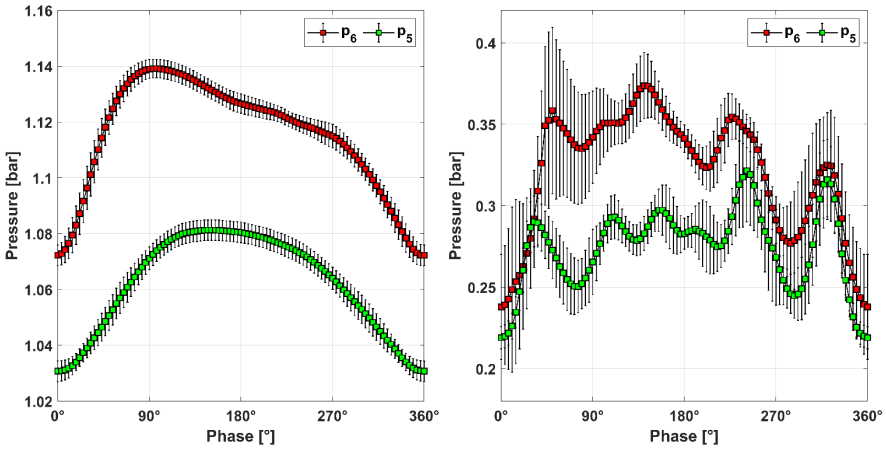


Figure 40: Phase-averaged pressure signals over the precession cycle at $n_{ED} = 0.343$ and $Q_{ED} = 0.176$. Left: non-cavitation conditions with a stable precessing vortex, Right: cavitation vortex rope at $\sigma = 0.09$ with upper part-load instability activated.

It is inferred from the results presented in Figure 40 (left) that for the non-cavitation precessing vortex, the flow structure should change significantly at the upper and lower measurement planes. Close to the turbine outlet ($p_5$), the pressure follows an almost symmetrical evolution in terms of the rise and decrease times. At the lower plane ($p_6$), however, this symmetry breaks and the pressure rise much faster than it takes it to decrease back to minimum (3/4 of the cycle). This interesting behavior could be explained by the average velocity fields that are shown in Figure 41. At the upper plane (left), the vortex core is more concentrated and possesses a relatively axisymmetric pattern compared to the lower plane (right). Given that the precession direction is counterclockwise, the vortex at the lower plane is preceded by an area with high tangential velocity compared to the upper plane. This accelerated flow contributes to a local depression that arrives at the sensor location before the vortex passage and can explain why the pressure decrease phase takes a longer potion of the cycle in the lower plane.

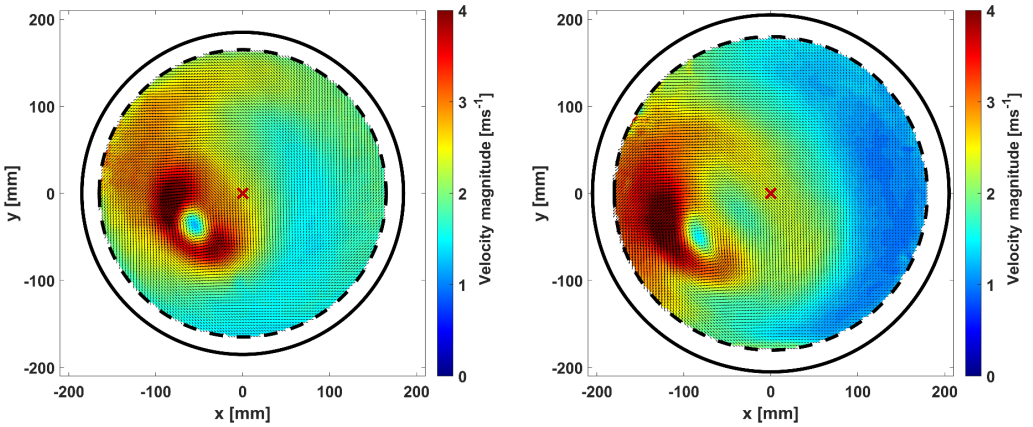


Figure 41: PIV contours in the upper and the lower planes of measurement ( $Q_{ED} / Q_{ED,BEP} = 0.80$ )

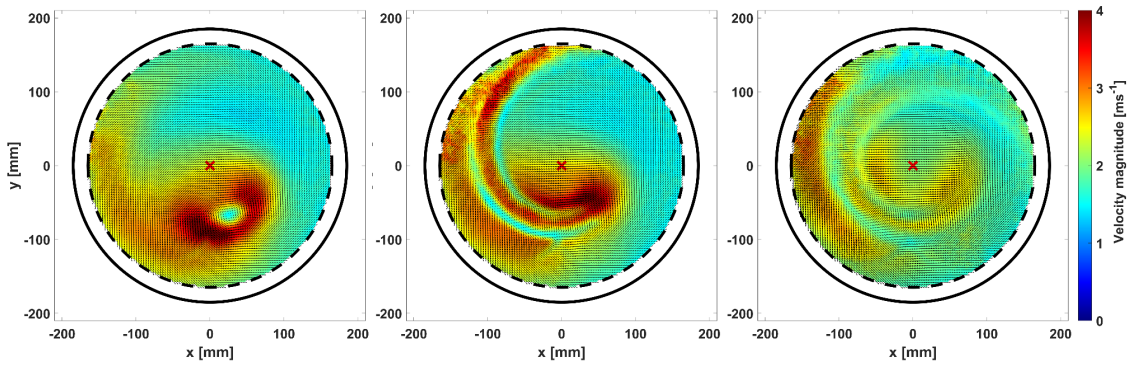


Figure 42: Phase-averaged velocity fields at $n_{ED} = 0.343$ and $Q_{ED} = 0.176$ for non-cavitation vortex (left) and cavitation vortices at $\sigma = 0.20$ (middle) and at $\sigma = 0.09$ (right).

The phase-averaged velocity fields measured at the upper plane for three values of cavitation number are presented in Figure 42. The image at left corresponds to the non-cavitation flow while the contours at the middle and right are obtained for cavitation vortices with $\sigma = 0.20$ and $\sigma = 0.09$, respectively. The cavitation vortex in the middle has a circular cross section while the one at right possesses an elliptical cross section. As a cavitation vortex partly blocks the PIV images and consequently the obtained velocity field, the vortex centers are not clear in the middle and right contours. It is perceived from the contours shown in Figure 42 that the occurrence of cavitation within the core of the vortex (comparison of the left and middle images) may first lead to a slight increase in the magnitude of the circumferential velocity. As the center of the vortex is occupied by vapor, whose angular momentum could be neglected compared to the liquid phase, the remaining swirl at the turbine outlet must be distributed over a lower surface area. It is harder to compare the result at $\sigma = 0.09$ with the two other points, as the cavitation vortex is quite large and blocks a considerable amount of the view. It may still be inferred that the velocity field is more diffused for the lowest value of cavitation number. Although the maximum of tangential velocity adjacent to the vortex core is diminished, it seems to have slightly increased at the larger radii.

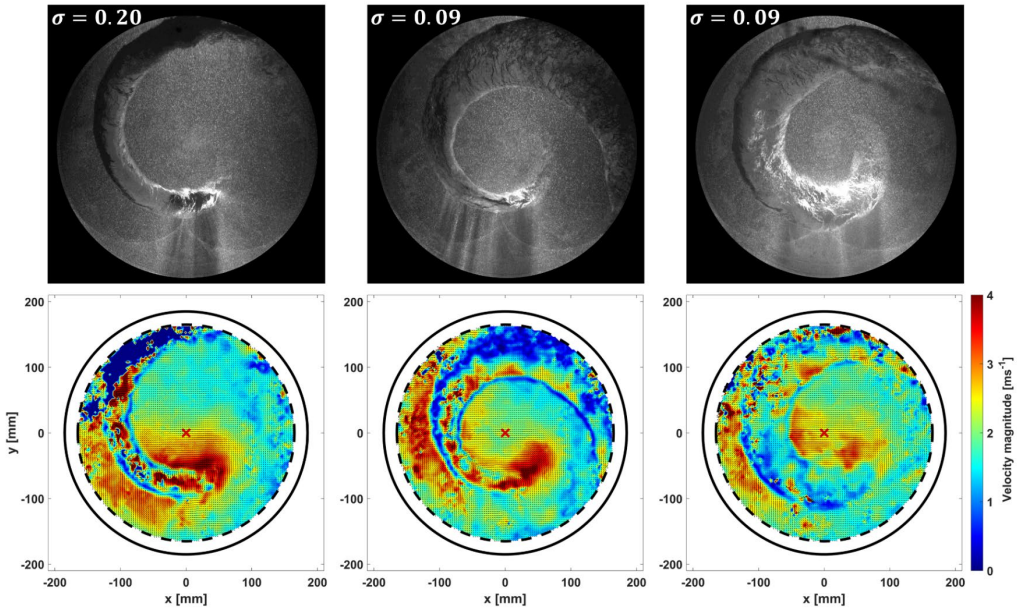


Figure 43: Instantaneous PIV moments and the corresponding velocity fields with the cavitation vortex rope at $Q_{ED} = 0.176$.

To achieve a better insight into the flow in the presence of cavitation, some PIV moments along with their instantaneous velocity fields are shown in Figure 43. The left picture corresponds to $\sigma = 0.20$ with circular vortex shape. The two other instants are associated with an elliptical vortex at $\sigma = 0.09$ where both pictures have been taken at the same phase of the precession cycle. All the pictures related to the circular vortex correspond to the same shape as presented in Figure 43. However, this does not hold for the elliptical vortex, as its state is not fully described only by the precession phase. As it is clear in Figure 43 (middle), at the moments when the elliptical vortex rope occupies a smaller volume, the velocity field surrounding it resembles much to the one of the circular vortex (the left contour). This includes the magnitude and the distribution pattern. On the contrary, when the elliptical vortex holds a larger volume in the plane of measurement, which could be due to a breathing effect, the velocity field alters in a way that the magnitude of the circumferential velocity decreases close to the vortex core and increases at farther positions. These results show that the phased-averaged velocities based on the precession do not represent the flow adequately in case of the upper part-load instability.

# 5 Conclusions

Within the scope of WP1, the first experimental campaign was conducted on a reduced-scale model of a Francis turbine installed on the EPFL PTMH test rig PF1, which was equipped with the flow excitation system. Several measurements were performed to compute the eigen frequencies of the test rig and to highlight the dependency of the hydro-acoustic response on the operational parameters of the machine. The results showed a clear response of the test rig to the excitation system and the value of the eigen frequency presented a relevant dependency on the discharge and the Froude number. The influence of these parameters is coherent with the previous studies in literature performed on different machines. Moreover, these results enabled the calibration of the SIMSEN model of the test rig and the investigated turbine to compute the hydro-acoustic parameters and predict the machine stability limits to accomplish the goals of WP2.

The measurements performed in the second phase of the experiments, within the framework of WP3, provided the unique opportunity of comparing the behavior of the same turbine in two test rigs. The obtained results reveal that, as predicted, the machine presents a relatively constant hydro-acoustic behavior, i.e. the computed key parameters follow the same trends when the operating conditions are varied. The exact values however change from one test rig to the other. For instance, the first eigen frequency shows a difference of maximum 30 % between the two test rigs. This observation could be attributed to the different layouts of the two test rigs. The velocity measurements performed in the second campaign helped to develop a much better understanding of the flow structures in the draft tube for the various operating conditions. This includes the part load and full load regimes as well as stable and unstable flow conditions. It has been shown how the variation of the Thoma number may affect the velocity field in the draft tube by triggering the upper part-load instability, which renders the vortex cross section elliptical and leads to high-amplitude high-frequency pressure fluctuations. The velocity fields were also used to explain the discharge variations during the full-load self-oscillation instabilities. In this work package, an image post-processing method was also developed to accurately estimate the volume of the cavitation vortex in the draft tube. Applying this method along with analyzing the data from dynamic modal analysis, a validation of the existing 1-D SIMSEN model of the EPFL PTMH PF3 was performed. Despite the satisfactory results acquired by the image processing and modal analysis, a full agreement between the volume-based method and the 1-D numerical model was not established, which requires further investigations.

# 6 Outlook and next steps

The results of the POST project have shed light on the issues related to the plant stability in off-design conditions. This project has also raised new unanswered questions through the following axes:

- The helical vortex structure with precession motion observed at full load, in contrast to the conventional cavitation structure, merits further investigations in terms of velocity field and instability analysis. Normally, the full-load regime is safe from a precession frequency and the self-oscillation only occurs for low values of the Thoma number. However, with this helical shape, the test rig suffers from the precession motion and the resulting vibrations even in full-load conditions, which directly affects its flexibility and stability.
- The elliptical shape of the vortex rope observed in the upper part-load instability requires further investigations to be clearly explained. As was shown in the report, the existing phase averaging method based on the main precession cycle is not capable of accurately detecting the flow structures in this flow conditions. Research should continue to define the trigger mechanism for this type of instability, too. As mentioned, there is the possibility of a breathing mechanism that should be explained by help of the high-speed videos. It seems that various modes of a vortex breakdown might play simultaneous roles in this phenomenon.
- It was shown in the report that the measured natural frequencies do not always coincide with those computed by SIMSEN. This could be attributed to the errors that might occur during the measurements or the post processing of the acquired data. For instance, the trace of the precession motion or any other sources of unwanted vibrations in the pressure signals may influence the accuracy of the calculated eigen frequencies of the test rig. This could also be due to the approximations and/or errors made in the estimation of the cavitation volume in the draft tube, which influence the accuracy of the predicted hydro-acoustic parameters. More investigations are required to address these issues correctly.

As is clear, further investigations should be performed to explain the mentioned open questions. Thanks to the two experimental campaigns, a relevant amount of data has been acquired for a wide range of

operating conditions of this Francis turbine. Although a considerable part of these data has already been analyzed and presented as a set of comprehensive results in this report, there remains some more to be investigated. Therefore, the post-processing of the acquired data is supposed to continue beyond the time scope of the project. The obtained results are expected to be published in scientific journals and presented in the upcoming conferences in the hydropower domain.

# 7 National and international cooperation

This research project was performed in collaboration with the following partners:

- Research partner: Waseda University, Research Institute for Science and Engineering, Miyagawa Laboratory (Tokyo, Japan).
- Industrial partner: Nippon Koei Co., Ltd., Power & Digital Business Unit, Sukagawa, Japan, for the provision of the reduced-scale model of the Francis turbine for the experimental campaigns.

# 8 Publications

**Published works:**

- R. Jacquod, ‘‘Study of the unsteady behavior of a Francis turbine’’, EPFL Master Thesis, January 2020.
- H. Dalbakken,” Characterization of the cavitation vortex rope stability in a Francis turbine at full load conditions”, EPFL Semester Project June 2020.
- M. Gilles, “Hydro-acoustic 1D simulation and modal analysis of a test rig featuring a Francis turbine”, EPFL Semester Project June 2020.
- B. Lahaye, “Velocity fields and hydroacoustic characteristics of the flow at instable full load operation of a Francis turbine”, EPFL Semester Project January 2021.
- E. Vagnoni, A. Favrel, J. Gomes Pereira Junior, A. Müller, K. Yamaishi, F. Avellan, “Influence of The Swirl Number on The Full Load Instability In Francis Turbines”, 21st International Seminar on Hydropower Plants VIENNA HYDRO 2020, Austria (postponed to 2022 due to COVID19).
- A. Favrel, E. Vagnoni, J. Gomes Pereira Junior, A. Müller, K. Yamaishi, F. Avellan and K. Miyagawa, “Dynamic behaviour of a full-load cavitation vortex in Francis turbine draft tube excited at its eigenfrequencies”, 30$^{th}$ IAHR Symposium on Hydraulic Machinery and Systems, Virtual Event, 2021.
- L.A. Alerci, “Modelling of the cavitation vortex rope in a Francis turbine at part load and full conditions”, EPFL Master Thesis, January 2021.
- A. Amini, E. Vagnoni, A. Favrel, K. Yamaishi, A. Müller and F. Avellan, “An experimental study on the upper part-load instability in a Francis turbine”, 30$^{th}$ IAHR Symposium on Hydraulic Machinery and Systems, Virtual Event, 2021.

**Under preparation:**

- E. Vagnoni, A. Amini, A. Favrel, J. Gomes, K. Yamaishi, A. Müller and F. Avellan, ‘‘Experimental study on the root causes and operational limits of the full-load instability in Francis turbines’’, prepared for Renewable Energy Journal, Elsevier.

- L.A. Alerci, E. Vagnoni, A. Amini, A. Favrel, K. Yamaishi, A. Müller, F. Avellan and M. Paolone, ‘‘Hydroacoustic response of the cavitation vortex rope at full-load condition in Francis turbines’’, prepared for Experiments in Fluids, Springer.
- A. Amini, E. Vagnoni, A. Favrel, K. Yamaishi, A. Müller and F. Avellan, “Cause and effect analysis of the upper part-load instability in Francis turbines” prepared for Experiments in Fluids, Springer.
- A. Amini, E. Vagnoni, A. Favrel, K. Yamaishi, A. Müller and F. Avellan, “Effect of swirl number on the velocity field of the flow in the draft tube of a Francis turbine” prepared for Renewable Energy, Elsevier.

# 9 References


[1] A. Müller, Physical Mechanisms governing Self-Excited Pressure Oscillations in Francis Turbines, EPFL PhD Thesis 6206, 2014.

[2] A. Favrel, Dynamics of the cavitation precessing vortex rope for Francis turbines at part-load operating conditions, EPFL PhD Thesis 6880, 2016.

[3] C. Landry, Hydro-acoustic Modeling of a Cavitation Vortex Rope for a Francis Turbine, EPFL PhD Thesis 6547, 2015.

[4] J. Gomes Pereira Jr, Predicting the dynamic behavior of Francis turbine generating units, EPFL PhD Thesis 7131, 2019.

[5] C. Landry et al., Local wave speed and bulk flow viscosity in Francis turbines at part-load operation, Journal of Hydraulic Research 54 (2) (2016) 185-196.

[6] A. Favrel et al. Dynamic modal analysis during reduced scale model tests of hydraulic turbines for hydro-acoustic characterization of cavitation flows. Mechanical Systems and Signal Processing 117 (2019) 81–96.

[7] C. Nicolet, Hydro-acoustic modelling, and numerical simulation of unsteady operation of hydroelectric systems, Ph.D. thesis, Lausanne (2007).

[8] C. Nicolet et al., New tool for the simulation of transient phenomena in Francis turbine power plants, in Proceedings of the Hydraulic Machinery and Systems 21st IAHR Symposium September 9-12, 2002, Lausanne, 2002.

[9] S. Alligné et al., Influence of the Francis turbine location under vortex rope excitation on the hydraulic system stability, International Journal of Fluid Machinery and Systems 2 (4) (2009) 286-294.

[10] S. Alligné et al., Cavitation surge modelling in Francis turbine draft tube, Journal of Hydraulic Research 52 (3) (2014) 399-411.

[11] A. Favrel et al., Prediction of hydro-acoustic resonances in hydropower plants by a new approach based on the concept of swirl number, Journal of Hydraulic Research 0 (0) (2019) 1-18.

[12] J. Gomes Pereira Jr et al, Procedure for predicting part-load resonance in Francis turbines hydropower units based on swirl number and local cavitation coefficient similitude, manuscript submitted for publication in Journal of Mechanical Systems and Signal Processing (2019).

[13] Swiss Federal Office of Energy SFOE. Schweizerische Elektrizitätsstatistik 2018, Statistique Suisse de l'Electricité 2018. Available online at https://www.bfe.admin.ch/bfe/de/home/versorgung/statistik-und-geodaten/energiestatistiken/elektrizitaetsstatistik.html

[14] Fisher, R. K., Palde, U., Ulith, P., 1980, "Comparison of draft tube surging of homologous scale models and prototype Francis turbines," In Proceeding of the 10th IAHR Symposium on Hydraulic Machinery and Systems (Tokyo, 1980), pp. 541-556.

[15] Dörfler, P. K., 1994, "Observation of the pressure pulsation on Francis model turbine with high specific speed," Hydropower & Dams (January 1994), 21-26.

[16] Nicolet, C., Zobeiri, A., Maruzewski, P. and Avellan, F., 2010, August. On the upper part load vortex rope in Francis turbine: Experimental investigation. In IOP Conference Series: Earth and Environmental Science (Vol. 12, No. 1, p. 012053). IOP Publishing.

[17] Koutnik, J., Krüger, K., Pochyly, F., Rudolf, P. and Haban, V., 2006, June. On cavitation vortex rope form stability during Francis turbine part load operation. In Proceedings of the first Meeting of the IAHR Int. Working Group on Cavitation and Dynamic Problems in Hydraulic Machinery and Systems (Barcelona (Vol. 304).

[18] Kirschner, O., Ruprecht, A. and Göde, E., 2009, October. Experimental investigation of pressure pulsation in a simplified draft tube. In Proceedings of the 3rd IAHR International Meeting of the Workgroup on Cavitation and Dynamic Problems in Hydraulic Machinery and Systems, Brno, Czech Republic (pp. 55-65).

[19] Favrel, A., Liu, Z., Takahashi, W., Irie, T., Kubo, M. and Miyagawa, K., 2019, December. Visualization of the elliptical form of a cavitation vortex rope and its collapse by two cameras. In IOP Conference Series: Earth and Environmental Science (Vol. 405, No. 1, p. 012035). IOP Publishing.